BIOPHYSICS

Molecular mechanism of extreme mechanostability in a pathogen adhesin

Lukas F. Milles,[1] Klaus Schulten,[2]* Hermann E. Gaub,[1]† Rafael C. Bernardi[2]†

High resilience to mechanical stress is key when pathogens adhere to their target and initiate infection. Using atomic force microscopy–based single-molecule force spectroscopy, we explored the mechanical stability of the prototypical staphylococcal adhesin SdrG, which targets a short peptide from human fibrinogen β. Steered molecular dynamics simulations revealed, and single-molecule force spectroscopy experiments confirmed, the mechanism by which this complex withstands forces of over 2 nanonewtons, a regime previously associated with the strength of a covalent bond. The target peptide, confined in a screwlike manner in the binding pocket of SdrG, distributes forces mainly toward the peptide backbone through an intricate hydrogen bond network. Thus, these adhesins can attach to their target with exceptionally resilient mechanostability, virtually independent of peptide side chains.

Gram-positive pathogenic bacteria have developed an arsenal of virulence factors specifically targeting and adhering to their host's proteins. Termed microbial surface components recognizing adhesive matrix molecules (MSCRAMMs), they promote "adhesion, invasion, and immune evasion" (1) (Fig. 1A). The prototypical adhesin is SD-repeat protein G (SdrG) from *Staphylococcus epidermidis*, the leading cause of medical device– and implant-related nosocomial infections (2). SdrG uses a key motif found in pathogenic staphylococci—the "dock, lock, and latch" (DLL) mechanism—in which the host target, usually a peptide on the order of 15 residues, is first bound (dock), then buried (lock) between two immunoglobulin-like (Ig) fold domains N2 and N3 (3). Finally, the target is snugly locked in place with a strand connecting N3 to N2 by β-strand complementation (latch) (Fig. 1B) (4). The DLL mechanism has appeared in many homologous domains—for example, in *Staphylococcus aureus* with targets such as keratin (5), complement system proteins (6), other chains of fibrinogen (7) and collagen (8). SdrG uses the DLL to target the N terminus of the β chain of human fibrinogen (Fg). The Fg sequence bound by SdrG is also the substrate of thrombin (Fgβ, NEEGFFSA**RG**HRPLD, thrombin cleavage between R and G). However, once bound by SdrG, it can no longer be cut by thrombin, a step necessary for blood clotting and fibrin formation (9). Thrombin cleavage also releases fibrinopeptide B, which in turn recruits neutrophils. Additionally, the adhesin coats and thus camouflages the bacterium in host proteins. Combined, these MSCRAMM mechanisms allow staphylococci to evade immune response, making

them attractive targets for drug development, such as designing MSCRAMM inhibitors for antiadhesion therapy (10, 11).

Here, we use the interplay between atomic force microscopy (AFM)–based single-molecule force spectroscopy (SMFS) (12–14) and all-atom steered molecular dynamics (SMD) simulations to elucidate the mechanics of the SdrG:Fgβ interaction with atomic resolution. Previous in vivo measurements using single-cell force spectroscopy of the SdrG fibrinogen interaction found adhesion forces on the order of 2 nN (15, 16); in addition, comparable in vivo forces appeared in closely related adhesins (17, 18). In agreement with these results, we measured rupture forces of more than 2 nN for a single SdrG:Fgβ complex at force loading rates around 10^5 pN s^{-1}. This extreme stability is the highest among all noncovalent interactions by a large margin. SdrG:Fgβ outperforms the current champion—the cohesin-dockerin type III interaction—by a factor of four (19) and Biotin-Streptavidin by more than an order of magnitude (20). It even rivals the strength of a covalent bond (21). Interestingly, the affinity between the peptide and SdrG is moderate, with a dissociation constant (K_d) ~400 nM (4). Accordingly, this system is adapted for strong mechanical attachment to its target, rather than high affinity. It was thus to be expected that these extreme SdrG:Fgβ mechanics were governed by a special, currently unknown mechanism.

The Fgβ wild-type (WT) peptide is located at the N terminus of the mature Fgβ chain. Thus, it can only be mechanically loaded from the C terminus (Fig. 1B). The SdrG N2 and N3 domains, responsible for binding the peptide (SdrG), are covalently anchored to the *S. epidermidis* cell wall by a C-terminal sortase motif. Hence, in the native, physiological configuration of the SdrG:Fgβ complex, force is applied from the C termini of both SdrG and Fgβ. To mechanically probe this interaction, all surface anchoring onto AFM cantilever and surface was site-specific and covalent (Fig. 1C). To ensure unambiguous identification of single-molecule events in force-extension traces, a refolding molecular "fingerprint" (22) was cloned

adjacent to the peptide. Under physiologically relevant direction of force application from the C terminus, the complex withstood extremely high forces of up to 2500 pN in vitro (Fig. 1, D and E) and even higher forces in corresponding SMD simulations (Fig. 1, F and G), due to higher force loading rates in silico (23, 24) (see also figs. S1 to S3).

The force regime around 2 nN is typically associated with the stability of covalent bonds, raising the concern that our surface chemistry—not the complex—was breaking, most likely a Si-C bond in the aminosilane anchors used (21). Because the cantilevers' apexes have radii of ~10 nm, they can only present a few molecules. If the covalent attachment of SdrG to the tip was being mechanically cleaved, the SdrG coating on the apex of the tip would be left attached to the surface, resulting in a rapidly decreasing frequency of interactions over time. In contrast, a single cantilever remained active over thousands of interactions, indicating that covalent bonds in the surface functionalization largely sustained the high forces.

We were convinced that an alteration that lowered the unbinding force would be the key to deconstructing the mechanism of this exceptional mechanostability. The presence of the "bulky" hydrophobic amino acid side chains of two phenylalanines (F) in Fgβ had been previously described as a "bulgy plug" (4). Buried behind the locking β strand, it seemed conceptually and intuitively plausible that wiggling them through the narrow constriction created by the locking strand caused the high forces (Fig. 2, A and B, and fig. S4).

The force dependence on the number of Fs was tested by addition of an F or by alanine replacement. Four constructs were investigated: a Fgβ with three phenylalanines (FgβF3), the WT Fgβ having 2 Fs, and mutants with one (FgβF1), or both (FgβF0), Fs replaced by alanines. The F3 mutant had been shown to have higher affinity (K_d ~50 nM) for SdrG (4), whereas the affinity of the F1 mutant was lower compared to WT Fgβ, because the F's hydrophobicity is important for initiating the DLL (25). All three mutants produced high forces around 2 nN (fig. S5, A and B). A negative correlation of the most-probable rupture force on the number of Fs was measurable but only marginal (Fig. 2C). With reference to the Fgβ WT force, the most-probable rupture force of the F0 mutant was only about 10% weaker than the WT. Multiple all-atom SMD simulations of all four systems reproduced the miniscule correlation between the presence of bulky F side chains and the high forces (Fig. 2B). The F0 mutant was ~20% weaker than WT Fgβ. Thus, the bulky residues only contributed marginally to the high forces, whereas they had been established as crucial for initial binding (4).

As the bulky phenylalanines in Fgβ were largely irrelevant for reaching high forces, we investigated minimizing the peptide. We employed QwikMD (26) to sequentially remove amino acids from the N terminus of Fgβ and tested their stability in SMD simulations. As expected, shortened peptides had lower unbinding forces. However,

[1]Lehrstuhl für Angewandte Physik and Center for Nanoscience, Ludwig-Maximilians-University, Amalienstrasse 54, 80799 Munich, Germany. [2]NIH Center for Macromolecular Modeling and Bioinformatics, Beckman Institute for Advanced Science and Technology, University of Illinois at Urbana-Champaign, Urbana, IL 61801, USA.
*Deceased.
†Corresponding author. Email: rcbernardi@ks.uiuc.edu (R.C.B.); gaub@lmu.de (H.E.G.)
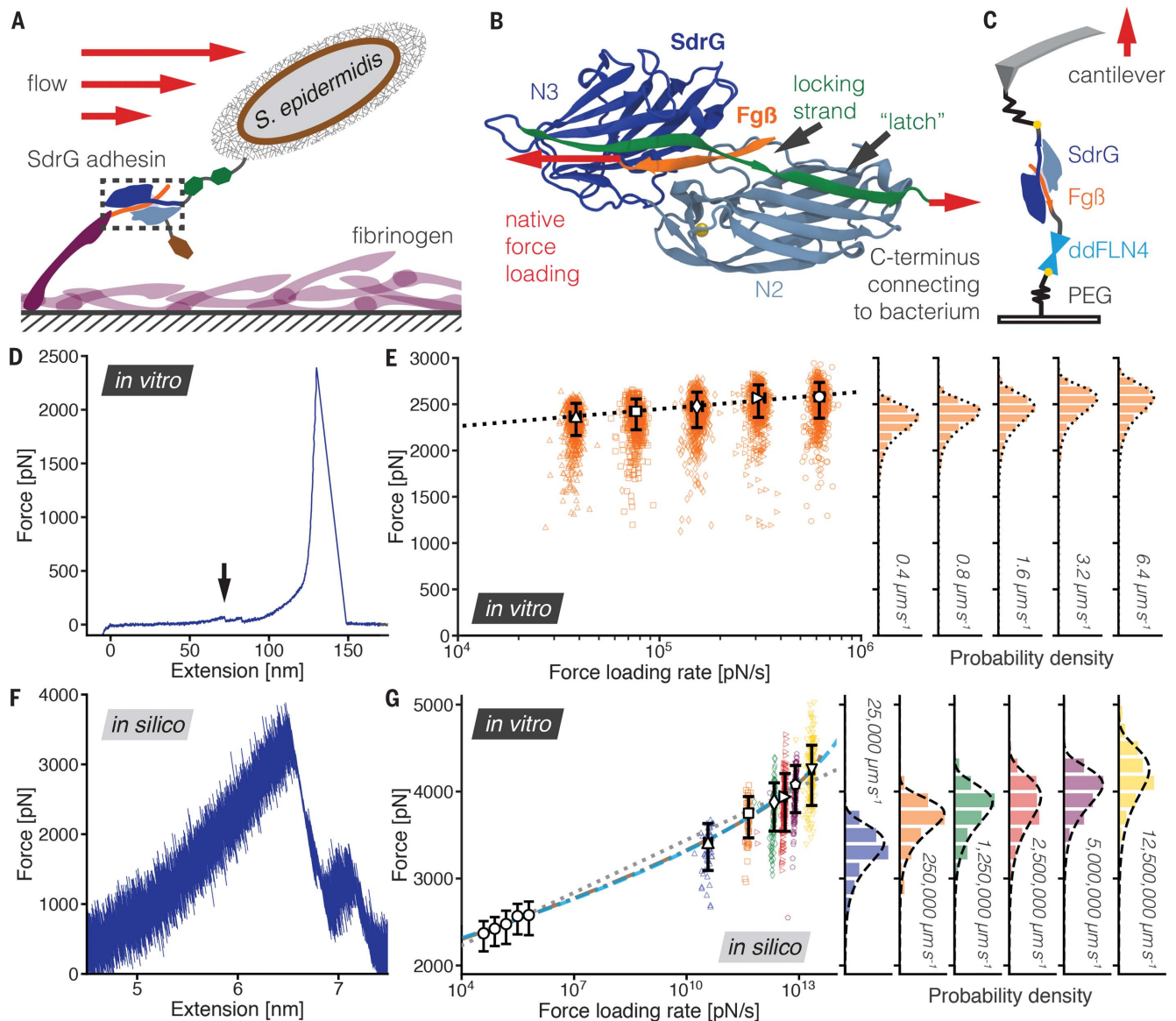
Fig. 1. The SdrG:Fgβ complex withstands enormous forces in vitro and in silico. (A) SdrG function, attached to the N-terminal peptide of the fibrinogen (purple) β chain (orange) adsorbed on a surface. This interaction prevents detachment of the bacterium by hydrodynamic forces. **(B)** Structure of the SdrG (blue):Fgβ (orange) complex. The locking strand (green) encloses the peptide in the binding pocket between the Ig-fold N2 (light blue) and N3 (dark blue) domain and a calcium (yellow) binding loop. The red arrows indicate the force applied to the molecular complex. **(C)** Experimental AFM setup, including the ddFLN4 fingerprint domain (cyan). All constructs are covalently bound to the surface via polyethyleneglycol (PEG) linkers and the ybbR-tag (yellow dots). In the native configuration, Fgβ and SdrG are force-loaded from their respective C termini. The AFM cantilever is retracted at constant velocity until the complex breaks. **(D)** Resulting force-extension trace in the native force propagation (blue), as it would occur at sites of staphylococcal adhesion. The distinctive fingerprint unfolding around 90 pN ddFLN4 (black arrow) featuring a substep was used to find specific interactions. It is followed by SdrG:Fgβ complex rupture, here at almost 2500 pN. **(E)** Dynamic force spectrum of the SdrG:Fgβ native geometry at cantilever retraction velocities 0.4 μm s^{-1} (triangles, N = 749), 0.8 μm s^{-1} (squares, N = 696), 1.6 μm s^{-1} (diamonds, N = 758), 3.2 μm s^{-1} (forward triangles, N = 749), 6.4 μm s^{-1} (circles, N = 851), with corresponding complex rupture-force histograms for each velocity projected onto individual axes on the right. A Bell-Evans (BE) model fit

(dotted line, Δx = 0.051 nm, k_{off}^0 = 9.2 × 10^{-11} s^{-1}) through the most-probable rupture force and force loading rate of each velocity (large open markers, with errors given as full-width at half maximum for each distribution) shows the expected force loading-rate dependency of the rupture force. **(F)** SMD force-extension trace (blue) in the native force propagation of SdrG:Fgβ, including experimental peptide linkers. The complex ruptured at almost 4000 pN; the extension is shorter than in the experimental trace because there are no PEG spacers. The peak following the highest force peak corresponds to another metastable geometry after slipping of the Fgβ peptide that is below the resolution limit of our AFM. **(G)** The experimentally determined dynamic force spectrum from velocities of 0.4 to 6.4 μm s^{-1} for the native propagation from (E) is shown condensed as open circles. The dynamic force spectrum of SMD simulations for velocities of 25,000 μm s^{-1} to 12,500,000 μm s^{-1}, triangle N = 49, square N = 50, diamond N = 100, forward triangle N = 200, pentagon N = 147, inverted triangle N = 200, respectively. Fits through SMD and experimental data, for BE model (gray, dotted line, Δx = 0.047 nm, k_{off}^0 = 1.0 × 10^{-9} s^{-1}) and fit of a model by Dudko et al. (DHS model, cusp potential Δx = 0.12 nm, k_{off}^0 = 6.1 × 10^{-22} s^{-1}, ΔG^{++} = 78 k_BT, cyan dashed line and linear-cubic potential Δx = 0.093 nm, k_{off}^0 = 7.7 × 10^{-18} s^{-1}, ΔG^{++} = 66 k_BT, brown dash-dotted line, both at T = 300 K). In vitro and in silico data agree exceptionally well, although they are separated by six orders of magnitude in force loading rate and can be fit with a single model.
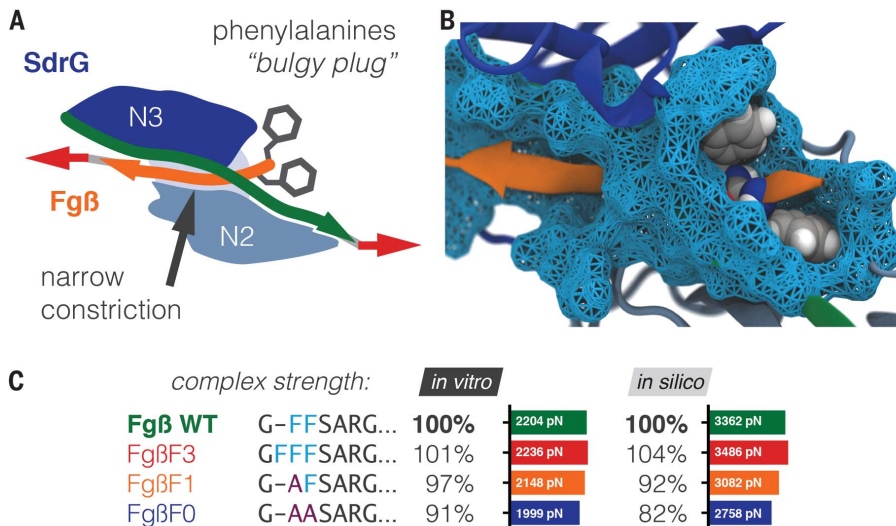
Fig. 2. Phenylalanine side chains only marginally influence SdrG:Fgβ mechanostability. (**A**) Sketch of the "bulgy plug" hypothesis. The bulky phenylalanine side chains (gray) of Fgβ (orange) are blocked by the locking strand (green). (**B**) Crystal structure showing the bulky phenylalanine side chains in van der Waals representation (gray spheres) of Fgβ (orange). They have to wiggle through a narrow constriction (cyan surface). (**C**) Dependence of complex rupture force on the presence of phenylalanines, if replaced by alanines. Most-probable rupture forces (absolute values in bar graphs) are compared relative to WT Fgβ. Either recorded experimentally with a single cantilever retracted at 1.6 μm s⁻¹ or corresponding results for SMD simulations at 250,000 μm s⁻¹. Adding one F (FgβF3 mutant) slightly increases forces. Yet, both results show a trend of weak dependence of rupture force on the presence of phenylalanines. Even when removing all bulky side chains (FgβF0 mutant), experimental rupture forces drop no more than 10% compared with WT Fgβ; in silico, no more than 20%. The "bulgy plug" only marginally contributes, hinting that another mechanism must be responsible for the high forces. Single-letter abbreviations for the amino acid residues are as follows: A, Ala; C, Cys; D, Asp; E, Glu; F, Phe; G, Gly; H, His; I, Ile; K, Lys; L, Leu; M, Met; N, Asn; P, Pro; Q, Gln; R, Arg; S, Ser; T, Thr; V, Val; W, Trp; and Y, Tyr.

provided that the peptide was long enough to directly interact with SdrG's locking strand, forces were still in the nN regime (Fig. 3A). Removing all residues contacting the locking strand up to Fgβ's A13 eliminated clear complex rupture forces in the nN regime. Consequently, the minimal six-residue peptide sequence in closest contact with the locking strand (FFSARG) was sufficient to both bind SdrG and withstand forces indistinguishable from WT Fgβ in vitro (Fig. 3B and fig. S5C).

Provided a mutant could still bind SdrG, modifying the Fgβ peptide had only minor effects on mechanostability. Thus, we investigated the mechanical properties of SdrG. Previously, the presence and flexibility of the locking strand was shown to be crucial for the DLL mechanism and thus SdrG:Fgβ affinity (25). Locking strand deletion inhibits binding of Fgβ (4). In accordance with these results, a mutant SdrG(274-580) devoid of the locking strand failed to bind Fgβ in vitro. Still, the contribution of the locking strand to the mechanics was unclear. If the interaction between the N2 domain and the locking strand propagated force away from the complex, its truncation should significantly weaken rupture forces. A truncated SdrG(274-590)—which removed the locking strand's C-terminal half of the "latch" region (fig. S6)—still bound SdrG, yet its mecha-

nostability was indistinguishable from the WT. Possible covalent isopeptide bonds (27, 28) between the locking strand and the N2 domain had been suggested to contribute to its stability. We could exclude this hypothesis as cause of the unusually high mechanostability because the SdrG truncation mutant removed D593, a key amino acid required for a potential isopeptide bond (29).

As simulations and experiments strongly agreed, we were confident to explore mutants and setups created in silico that could not be realized in vitro. SMD became a gedankenexperiment to deconstruct the mechanism. It is important to emphasize that the strong agreement was provided in part by our enhanced sampling strategy (30). Performing many (at least 50 per system, more than 2400 total; see overview in table S1) simulation replicas allowed the comparison of simulation and experiment within the same theoretical framework of the Bell-Evans (BE) and Dudko-Hummer-Szabo (DHS) models (24, 31, 32).

Simulations revealed the presence of strikingly frequent and persistent hydrogen bonds (H bonds) between the Fgβ peptide backbone and SdrG (Fig. 3, D and F, and figs. S7 and S8). We investigated the contribution of the backbone H bonds in SMD simulations by replacing Fgβ with a polyglycine peptide, which has no side chains.

In silico, the rupture forces were merely 27% weaker than the WT, comparable to the FgβF0 mutant (Fig. 3E). Thus, we updated our initial hypothesis: Reaching the regime of 2 nN was largely independent of Fgβ's side chains and mainly caused by SdrG interacting with the Fgβ peptide backbone (figs. S9 and S10). Breaking the SdrG:Fgβ complex in the native configuration requires all H bonds to be broken in parallel: a cooperative shear geometry (see movie S1).

Similar shear geometries appear in folds such as the muscle protein titin-Ig. However, this protein unfolds at lower forces around 200 pN (33), in stark contrast to SdrG's over 2000 pN. The shear geometry in titin breaks because its backbone H bonds have the freedom to move orthogonally to the force load, ultimately circumventing the shear geometry (34). In the SdrG:Fgβ complex, the peptide is snugly confined in the interface between N2 and N3 domain by the locking strand (figs. S10 and S11). The rigid and coiled (Fig. 3C and fig. S12) alignment of the two interacting backbones neither bends nor buckles. Peptide movement orthogonal to the pulling force vector is not possible, so all H bonds must be broken at once. The importance of this packed confinement was also demonstrated by analyzing the correlation-based dynamical network (35), which shows how force propagates through the system (fig. S13) and how atom motion is clustered in communities (fig. S14). These analyses revealed that force is propagated not directly by the latch strand, as demonstrated experimentally, but by neighboring strands, reducing the load over the H bonds. Notably, the movement of the Fgβ peptide and both the N2 and N3 domain were highly correlated. To demonstrate the importance of the correct H-bond alignment, Fgβ was tethered non-natively from its N terminus, effectively pulling orthogonally to the native force propagation. The non-native pulling of Fgβ peaked at forces around 60 pN (Fig. 4A), smaller than the native configuration by a factor of more than 40 (fig. S15). Simulations showed that this geometry is weaker, because the interactions between N2 and N3 are broken, resulting in a loss of peptide confinement (see figs. S16 and S17, and movie S2).

In a simplified model, the DLL mechanism creates a deep and rigid binding pocket for the peptide, which is confined in a coiled geometry similar to a corkscrew in a cork (figs. S12 and S18). If pulled upon, the load is dissipated cooperatively over all H bonds that are radially pointed outward of Fgβ (Fig. 3G), causing the high mechanostability.

The importance of these H bonds was confirmed in an exploratory SMD through removing coulomb interactions from parts of the peptide required for hydrogen bonding. Eliminating backbone H bonds resulted in a significant reduction in rupture force in silico (Fig. 3E). Additionally, eliminating hydrogen bonds formed by the side chains of Fgβ further reduced the forces, but only marginally, in agreement with the mechanism proposed (Fig. 3E). Still, the forces observed were only about 40% smaller than the WT. Furthermore, we tested turning off H bonds of the all-glycine peptide, which finally led to
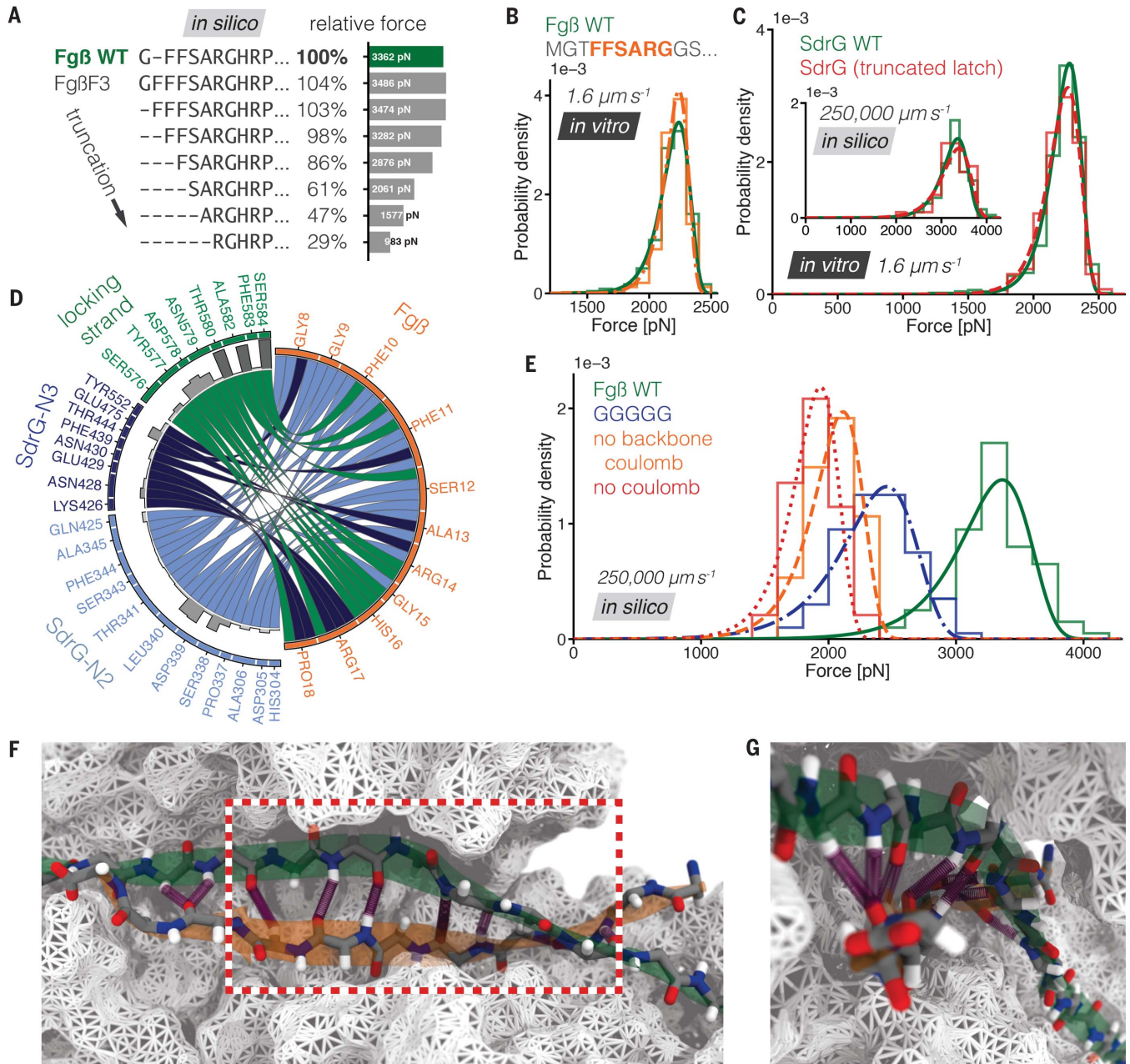
Fig. 3. Backbone H bonds are deciding factors in the high mechanostability of SdrG:Fgβ and a minimized peptide. (**A**) Fgβ peptide truncations from the N terminus in silico. Removing amino acids causes the forces to drop (relative to the WT), with the most significant drop when removing the sequence FSAR, leading to FFSARG as the minimum peptide. (**B**) Rupture forces for SdrG binding to WT Fgβ (green, continuous line, N = 437), and the six-residue minimized peptide FFSARG (orange, dash-dotted line, here shown with surrounding amino acids in gray, N = 471). Strikingly, there is hardly any difference between WT Fgβ and the minimized peptide. (**C**) Rupture-force histograms comparing the WT Fgβ:SdrG interaction (green, continuous line, N = 463) and the SdrG mutant with the truncated latch region (red, dashed line, N = 131). WT and mutant are virtually indistinguishable (no significant difference in Kolmogorov-Smirnov test, in vitro P = 0.29, in silico P = 0.88). Corresponding SMD results (WT N = 100, mutant N = 50) are shown as inset. (**D**) Relative prevalence (bar graphs;

precise values in fig. S7) of H bonds between SdrG domains, the locking strand, and the WT Fgβ peptide (also available for F3, F1, F0, and all-glycine mutants in fig. S8). The locking strand connects to nearly every Fgβ residue. (**E**) Rupture forces from exploratory simulations for SdrG and Fgβ WT (green, continuous line, N = 100), a replacement of each Fgβ residue with glycine (blue, dash-dotted line, N = 100), FgβF3 peptide without coulomb interactions, and subsequently H bonds, on its backbone (orange, dashed line, N = 47), FgβF3 devoid of all coulomb interactions (red, dotted line, N = 48). Backbone H bonds in the Fgβ confinement allow even a pure glycine sequence to withstand high force. (**F**) H-bond (purple) contacts respective to the backbone of Fgβ (orange) and locking strand (green) confined by SdrG (white surface) from simulations in a force-loaded state. The minimum peptide sequence is highlighted in the red box. (**G**) Radial distribution of backbone H bonds between locking strand (green) caused by the screwlike winding of the Fgβ sheet (orange). Peptide backbones are shown as sticks.
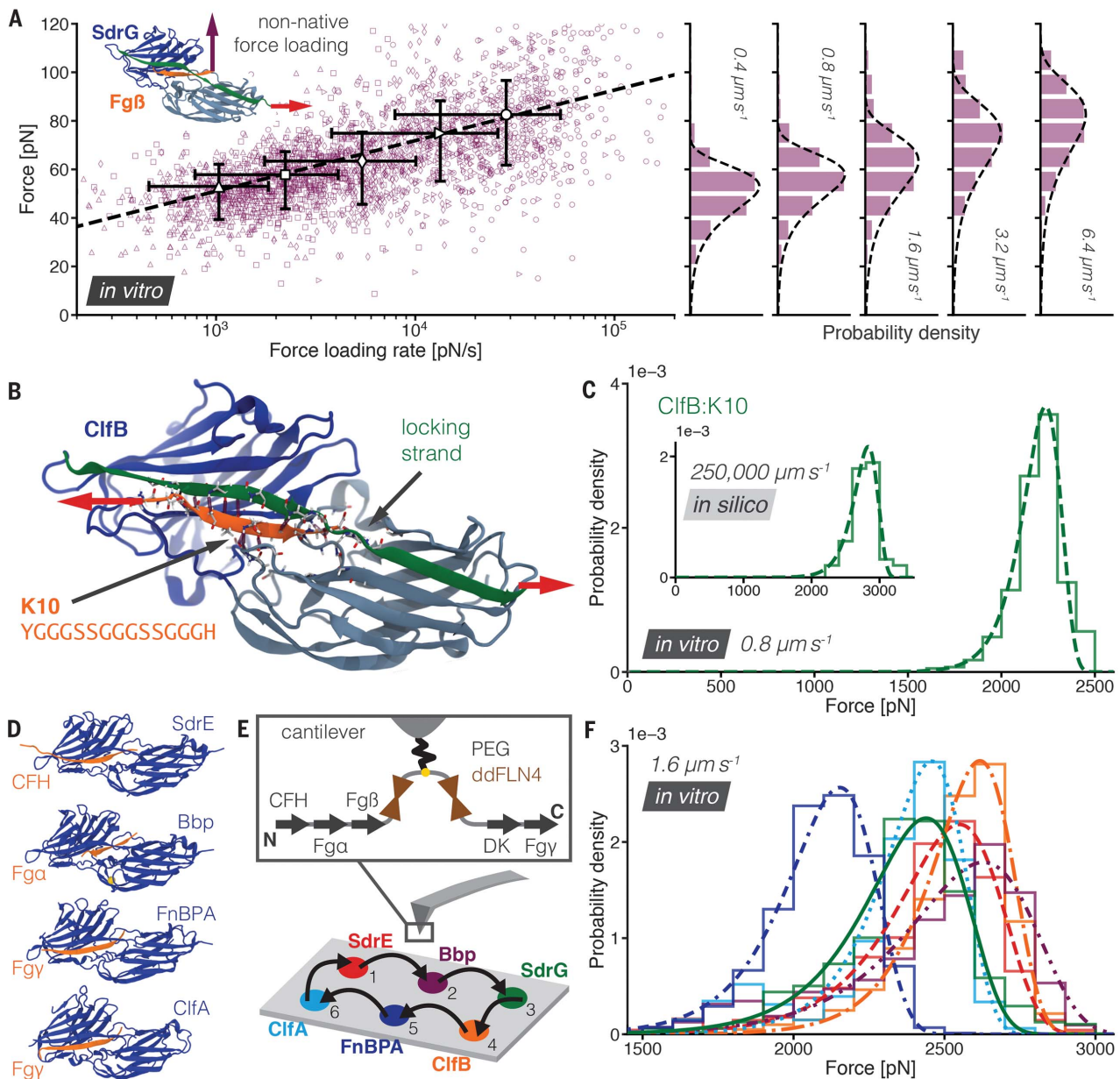
Fig. 4. A non-native SdrG:Fgβ force loading shows weak forces, a homologous domain ClfB reaches 2 nN stability binding a mainly glycine-serine peptide, and SdrG homologs consistently exceed 2 nN binding to their ligands. (**A**) Dynamic force spectrum of the SdrG:Fgβ non-native configuration (see inset with purple arrow), breaking around 60 pN as opposed to >2 nN for the native case (for SMD results, see figs. S15 to S17 and movie S2). Cantilever retraction velocities were varied: 0.4 μm s^{-1} (triangles, N = 511), 0.8 μm s^{-1} (squares, N = 564), 1.6 μm s^{-1} (diamonds, N = 487), 3.2 μm s^{-1} (forward triangles, N = 395), 6.4 μm s^{-1} (circles, N = 471), with corresponding complex rupture-force histograms projected on the right. A BE model fit (dashed line) through the most-probable rupture force and force loading rate of each velocity (large open markers) shows the expected force loading-rate dependency of the rupture force (Δx = 0.46 nm, k_{off}^0 = 0.39 s^{-1}). (**B**) ClfB (blues):K10 (orange) complex, including the locking strand (green) and H-bonding (purple) amino acids, shown as sticks. Notably, the latch region was not crystallized and needed to be modeled from a homolog. The native pulling configuration is indicated with an arrow; compared with Fgβ, the peptide is oriented inversely in the binding pocket. (**C**) Rupture-force histogram and fit for ClfB:K10 at a velocity of 0.8 μm s^{-1} (green, dashed line,

N = 1035), peaking around 2.3 nN. Simulation data (N = 50) confirming the force regime are shown as inset. (**D**) Homologous systems employing the DLL mechanism, all from *S. aureus* (N2 and N3 domains in blue, target peptides in orange) SdrE, Bbp, FnBPA, and ClfA. (**E**) Comparison of absolute mechanostability of all homologous systems, as well as SdrG and ClfB, with a single force probe. The cantilever is modified with five different peptides tethered in their native force loading geometry, respectively: from the C terminus of complement factor H (CFH), Fgα chain (Fgα), and Fgβ, tethered from the N terminus are sequences from dermokine (DK) and Fgγ chain (Fgγ). This selection is presented to all adhesins, which are known to bind at least one of them, spatially separated on a surface. One cannot exclude that one adhesin may bind more than one peptide target. (**F**) Resulting relative stabilities of the complexes for SdrE (red, dashed line, N = 680), ClfB (orange, dash-dotted line, N = 605), ClfA (cyan, dashed line, N = 2292), Bbp (purple, dot-dot-dashed line, N = 319), SdrG (green, continuous line, N = 478), FnBPA (blue, dash-dash-dotted line, N = 2483). SdrG is not the strongest system at a retraction velocity of 1.6 μm s^{-1}. In accordance with the largely side-chain independent mechanics proposed for SdrG and ClfB, every DLL adhesin withstands forces exceeding 2 nN.

no detectable peak in the force profile. H bonds with the peptide backbone were key to the mechanostability.

A pure glycine sequence—i.e., no side chains—showed high forces when bound to SdrG in silico. An analogous experiment was not possible, because such a sequence did not bind SdrG. The side chains, such as the hydrophobic phenylalanine residues, were not essential for mechanostability but were crucial for affinity. A homologous DLL motif adhesin, clumping factor B (ClfB) from *S. aureus,* had been found to promiscuously bind short sequences of extracellular matrix proteins. Among its targets is a C-terminal cytoskeletal keratin peptide (K10, YGGGSSGGGSSGGGH.) (*5*). This unusually unremarkable target is essentially a flexible linker terminating in a charged residue. K10 contains no bulky, charged, or hydrophobic side chains, except for the C-terminal histidine, secured by the locking strand in the complex structure. ClfB:K10 interactions also exceed the 2 nN mark, both in vitro and in silico (see Fig. 4, B and C). More prominently than in SdrG, ClfB's mechanostability must be based on H bonds to the K10 backbone, simply because it has no notable side chains. In last consequence, even a shortened K10 and pure GS sequence (GGGSSGGGSSGGG) binds ClfB and reaches more than 2nN in force (fig. S19). Moreover, the peptide β sheet is parallel to the locking strand, whereas the orientation is antiparallel in SdrG. Accordingly, it was natively tethered from its N terminus, showing that nN stability is also possible for an inversely oriented peptide configuration. Finally, to generalize the mechanics, we probed four additional homologs of SdrG and ClfB, all from *S. aureus.* SD repeat protein E (SdrE), clumping factor A (ClfA), bone sialoprotein binding protein (Bbp), and fibronectin binding protein A (FnBPA) had been crystallized with a known ligand bound (Fig. 4D) (*36–39*). Although most-probable rupture forces varied up to 20% depending on the adhesin, the overall forces were consistently in the 2 nN regime (Fig. 4, E and F).

Side-chain independent mechanics confer an invasive advantage to staphylococci. No matter which sequence is targeted by their adhesins, invading pathogens using the DLL mechanism can adhere to their hosts even under the most demanding mechanical stress. One could speculate that this mechanism provides a flat fitness landscape. Adaption to a target will automatically yield extremely resilient mechanics, even if the sequence is mainly glycines and serines. The moderate bulk affinity of SdrG:Fgβ allows for flexible unbinding and rebinding when no mechanical stress is applied. One could further speculate that a high-complex lifetime under force, which seems probable given the overall extreme mechanostability, is indicative of a very different unbinding pathway when compared with the moderate lifetimes of spontaneous unbinding in bulk experiments (*4*). Thus, these differing pathways would make a catch-bond behavior not surprising, considering that such bonds have been found in bacterial adhesins with similar functions, albeit much lower mechanical strength (*40, 41*).

In conclusion, SdrG:Fgβ and its homologs are the mechanically strongest noncovalent protein-protein receptor-ligand interactions to date, rivaling a regime formerly exclusively associated with covalent bonds. The DLL mechanism creates a deep and rigid binding pocket confining the target in a stable geometry that mainly relies on backbone H bonds. Hence, the mechanostability of the complex only marginally depends on the target side chains and thus sequence, even if it is minimized to merely six amino acids. These adhesins are hyperstable protein handles suitable for mechanochemistry and able to unfold almost any protein. They may serve as templates to design even stronger ones—a noncovalent superglue (*42, 43*). The mechanism proposed provides an atomistic understanding of why these adhesins can adhere to their hosts so resiliently, from which possible routes to inhibit it and impede staphylococcal adhesion may be derived.

REFERENCES AND NOTES

1. T. J. Foster, J. A. Geoghegan, V. K. Ganesh, M. Höök, *Nat. Rev. Microbiol.* **12**, 49–62 (2014).
2. M. Otto, *Nat. Rev. Microbiol.* **7**, 555–567 (2009).
3. C. C. S. Deivanayagam et al., *EMBO J.* **21**, 6660–6672 (2002).
4. K. Ponnuraj et al., *Cell* **115**, 217–228 (2003).
5. V. K. Ganesh et al., *J. Biol. Chem.* **286**, 25963–25972 (2011).
6. J. A. Sharp et al., *PLOS ONE* **7**, e38407 (2012).
7. T. J. Foster, M. Höök, *Trends Microbiol.* **6**, 484–488 (1998).
8. Y. Zong et al., *EMBO J.* **24**, 4224–4236 (2005).
9. S. L. Davis, S. Gurusiddappa, K. W. McCrea, S. Perkins, M. Höök, *J. Biol. Chem.* **276**, 27799–27805 (2001).
10. H. Breithaupt, *Nat. Biotechnol.* **17**, 1165–1169 (1999).
11. J. A. Geoghegan, T. J. Foster, P. Speziale, Y. F. Dufrêne, *Trends Microbiol.* **25**, 512–514 (2017).
12. D. J. Müller, Y. F. Dufrêne, *Nat. Nanotechnol.* **3**, 261–269 (2008).
13. V. Vogel, M. Sheetz, *Nat. Rev. Mol. Cell Biol.* **7**, 265–275 (2006).
14. H. Yu, M. G. W. Siewny, D. T. Edwards, A. W. Sanders, T. T. Perkins, *Science* **355**, 945–950 (2017).
15. P. Herman et al., *Mol. Microbiol.* **93**, 356–368 (2014).
16. T. Vanzieleghem, P. Herman-Bausier, Y. F. Dufrene, J. Mahillon, *Langmuir* **31**, 4713–4721 (2015).
17. P. Vitry et al., *mBio* **8**, e01748–e17 (2017).
18. P. Herman-Bausier et al., *mBio* **7**, e01529–e16 (2016).
19. C. Schoeler et al., *Nat. Commun.* **5**, 5635 (2014).
20. R. Merkel, P. Nassoy, A. Leung, K. Ritchie, E. Evans, *Nature* **397**, 50–53 (1999).
21. M. Grandbois, M. Beyer, M. Rief, H. Clausen-Schaumann, H. E. Gaub, *Science* **283**, 1727–1730 (1999).
22. I. Schwaiger, A. Kardinal, M. Schleicher, A. A. Noegel, M. Rief, *Nat. Struct. Mol. Biol.* **11**, 81–85 (2004).
23. F. Rico, L. Gonzalez, I. Casuso, M. Puig-Vidal, S. Scheuring, *Science* **342**, 741–743 (2013).
24. O. K. Dudko, G. Hummer, A. Szabo, *Phys. Rev. Lett.* **96**, 108101 (2006).
25. M. G. Bowden et al., *J. Biol. Chem.* **283**, 638–647 (2008).
26. J. V. Ribeiro et al., *Sci. Rep.* **6**, 26536 (2016).
27. M. Walden et al., *eLife* **4**, 1–24 (2015).
28. J. Alegre-Cebollada, C. L. Badilla, J. M. Fernández, *J. Biol. Chem.* **285**, 11235–11242 (2010).
29. U. Sridharan, K. Ponnuraj, *Biophys. Rev.* **8**, 75–83 (2016).
30. R. C. Bernardi, M. C. R. Melo, K. Schulten, *Biochim. Biophys. Acta* **1850**, 872–877 (2015).
31. E. Evans, K. Ritchie, *Biophys. J.* **72**, 1541–1555 (1997).
32. S. Izrailev, S. Stepaniants, M. Balsera, Y. Oono, K. Schulten, *Biophys. J.* **72**, 1568–1581 (1997).
33. M. Rief, M. Gautel, F. Oesterhelt, J. M. Fernandez, H. E. Gaub, *Science* **276**, 1109–1112 (1997).
34. H. Lu, K. Schulten, *Biophys. J.* **79**, 51–65 (2000).
35. C. Schoeler et al., *Nano Lett.* **15**, 7370–7376 (2015).
36. X. Zhang et al., *Protein Cell* **6**, 757–766 (2015).
37. Y. Zhang et al., *Biochem. J.* **474**, 1619–1631 (2017).
38. V. Stemberk et al., *J. Biol. Chem.* **289**, 12842–12851 (2014).
39. V. K. Ganesh et al., *PLOS Pathog.* **4**, e1000226 (2008).
40. W. E. Thomas, V. Vogel, E. Sokurenko, *Annu. Rev. Biophys.* **37**, 399–416 (2008).
41. M. M. Sauer et al., *Nat. Commun.* **7**, 10738 (2016).
42. G. Veggiani, B. Zakeri, M. Howarth, *Trends Biotechnol.* **32**, 506–512 (2014).
43. T. Verdorfer et al., *J. Am. Chem. Soc.* **139**, 17841–17852 (2017).

Science

Molecular mechanism of extreme mechanostability in a pathogen adhesin

Lukas F. Milles, Klaus Schulten, Hermann E. Gaub and Rafael C. Bernardi

How a pathogen holds on to its host

Staphylococcus epidermidis and *Staphylococcus aureus* are pathogens that can form biofilms on implants and medical devices. Central to biofilm formation is a very tight interaction between microbial surface proteins called adhesins and components of the extracellular matrix of the host. Milles *et al.* used atomic force microscopy-based single-molecule force spectroscopy combined with steered molecular dynamics to explore how the bond between staphylococcal adhesin SdrG and its target fibrinogen peptide can withstand forces greater than 2 nanonewtons (see the Perspective by Herman-Bausier and Dufrêne). The peptide is confined in a coiled geometry in a deep and rigid pocket through hydrogen bonds between SdrG and the peptide backbone. If pulled, the load is distributed over all hydrogen bonds so that all bonds must be broken at once to break the interaction.
Science, this issue p. 1527; see also p. 1464

Supplementary Materials for

Molecular mechanism of extreme mechanostability in a pathogen adhesin

Lukas F. Milles, Klaus Schulten, Hermann E. Gaub,* Rafael C. Bernardi*

*Corresponding author. Email: rcbernardi@ks.uiuc.edu (R.C.B.); gaub@lmu.de (H.E.G.)

This PDF file includes:

Materials and Methods
Figs. S1 to S19
Table S1
References

Other Supplementary Material for this manuscript includes the following:
(available at www.sciencemag.org/cgi/content/full/359/6383/1527/DC1)

Movies S1 and S2

Materials and Methods

All chemicals used were supplied by Carl Roth (Karlsruhe, Germany) or Sigma-Aldrich (St. Louis, MO, USA) if not specified explicitly.

Gene construction

The *Dictyostelium discoideum* 4th filamin domain (ddFLN4, UniProt: P13466, residues 549 - 649), the *Staphylococcus epidermidis* SdrG N2 and N3 domain genes, as well as *Staphylococcus aureus* N2 and N3 domains of: ClfB, SdrE, ClfA, Bbp, FnBPA (full sequences and UniProt accession numbers below) were synthesized codon-optimized for expression in *Escherichia Coli* as linear DNA fragments (GeneArt – ThermoFisher Scientific, Regensburg, Germany) with suitable overhangs. Genes were cloned into pET28a Vectors with a hexahistidine- and ybbr-tag using the Gibson assembly strategy (*1*) (New England Biolabs, MA, USA). The C18S mutation in the ddFLN4 and all other amino acid point mutations, deletions or additions in the Fg as well as K10 peptides and SdrG protein were introduced by blunt end ligation cloning using T4 Ligase (Thermo Scientific, MA, USA). Final open reading frames of all constructs were checked by DNA sequencing (Eurofins Genomics, Ebersberg, Germany). The complete sequences of all protein constructs used are listed below.

Key plasmids were deposited with and can be ordered from Addgene (www.addgene.org):

Plasmid	AddgeneID
pET28a-SdrG_N2N3-HIS-ybbr	101238
pET28a-Fgß-ddFLN4-HIS-ybbr	101239
pET28a-FFSARG-ddFLN4-HIS-ybbr	101240
pET28a-ClfB_N2N3-HIS-ybbr	101717
pET28a-ybbr-HIS-ddFLN4-K10	101718
pET28a-ybbr-HIS-ddFLN4-Fgß	101719
pET28a-FgßF3-ddFLN4-HIS-ybbr	101743

Protein expression and purification

Proteins were expressed ybbr-tagged and 6xHIS-tagged (*2*). All proteins were expressed in *E. Coli* NiCo21(DE3) (New England Biolabs, MA, USA). Precultures of 5 mL in LB medium containing 50 μg/mL Kanamycin, grown overnight at 37° C, were inoculated in 200 mL of ZYM-5052 autoinduction media (*3*) containing 100 μg/mL Kanamycin and grown for 6 h at 37° C and then overnight at 18° C. Bacteria were harvested by centrifugation at 8000 g, and pellets were stored frozen at -80° C until purification.

All purification steps were performed at 4 to 8° C. The bacterial pellet was resuspended in Lysis Buffer (50 mM TRIS, 50 mM NaCl, 5 mM MgCl$_2$, 0.1% (v/v) TritonX-100 or 0.1% (v/v) Tween-20, 10% (v/v) Glycerol, pH 8.0) including 100 μg/mL Lysozyme (Carl Roth, Karlsruhe, Germany) and cells were lysed through sonication (Sonoplus GM 70, with a microtip MS 73, Bandelin, Berlin, Germany) followed by centrifugation at 40000 g for 45 min. The supernatant was applied to a Ni-NTA column (HisTrap FF 5mL on a Äkta Start system, both GE Healthcare, MA, USA) for HIS-Tag purification and washed extensively (25 mM TRIS, 500 mM NaCl, 20 mM Imidazole,

0.25 % (v/v) Tween-20, 10 % (v/v) Glycerol, pH 8.0). The protein was eluted in the same buffer supplemented with 200 mM imidazole. Protein containing fractions were concentrated in centrifugal filters (Amicon, Merck, Darmstadt, Germany), exchanged into measurement buffer (TBS: 25 mM Tris, 150 mM NaCl, pH 7.4) by desalting columns (Zeba, Thermo Scientific, MA, USA), and frozen in aliquots with 10 % (v/v) glycerol in liquid nitrogen to be stored at -80° C until used in experiments. Protein concentrations were measured by spectrophotometry at 280 nm with typical final concentrations of 30 - 1000 µM (on a NanoDrop 1000, Thermo Scientific, DE, USA).

AFM sample preparation

Detailed AFM-SMFS protocol have been published previously (*4*, *5*). In brief, AFM Cantilevers (Biolever Mini AC40TS, Olympus, Tokyo, Japan) and 24 mm diameter cover glass surfaces (Menzel Gläser, Braunschweig, Germany) were modified with Aminosilane.

Glass surfaces: glass surfaces were cleaned by sonication in 50% (v/v) 2-propanol in ultrapure H_2O for 15 min. Subsequently, surfaces were oxidized in 50% (v/v) H_2O_2 and 50% (v/v) of 30% (v/v) sulfuric acid for 30 min. Surfaces were washed in ultrapure H_2O, dried in a gentle stream of nitrogen before being silanized by soaking in (3-Aminopropyl) dimethylethoxysilane (ABCR, Karlsruhe, Germany) 1.8% (v/v) in Ethanol for 1 h. Followed by washing in 2-propanol twice and baking at 80° C for 1 h. Glass surfaces were stored under Argon and used within one month.

Cantilevers: after 15 min of UV-Ozone cleaning (UVOH 150 LAB, FHR Anlagenbau GmbH, Ottendorf-Okrilla, Germany), cantilevers were incubated in 1 mL (3-aminopropyl)-dimethyl-ethoxysilane (APDMES, abcr, Karlsruhe, Germany) mixed with 1 mL Ethanol and 5 µL H_2O for 5 min, followed by rinsing in Ethanol and subsequently in ultrapure water. Cantilevers were then baked at 80° C for 1 h to be stored overnight under Argon and used the next day.

Two protocols for producing glass surfaces and cantilevers covered in CoA-terminated Polyethylene glycol (PEG) molecules were used:
- Both glass surfaces and cantilevers were covered with 5 kDa heterobifunctional α-Maleinimidohexanoic-PEG-NHS (Rapp Polymere, Tübingen, Germany) dissolved in 50 mM HEPES (pH 7.5) at 25 mM (125 mg/mL) for 30 min. After rinsing surfaces and cantilevers in ultrapure water, 1 mM Coenzyme A (in 50 mM sodium phosphate pH 7.2, 50 mM NaCl, 10 mM EDTA buffer) was applied to both for at least 1 h.
- Both glass surfaces and cantilevers were covered with 5 kDa heterobifunctional NHS-PEG-Acrylate (JenKem Technology, Spring Creek, TX, USA) dissolved in 50 mM HEPES (pH 7.5) at 20 mM (100 mg/mL) for 1 h. After rinsing surfaces and cantilevers in ultrapure water, both were covered with 1 mM Coenzyme A (in 50 mM sodium phosphate pH 7.2, 50 mM NaCl, 10 mM EDTA, degassed). Samples were placed in a Nitrogen atmosphere and placed approximately 1-2 cm from an LED emitting at 365 nm wavelength (LZ1-10UV00 LED array, LedEngin, Santa Clara, CA). Irradiation occurred directly with ultraviolet light to induce Coupling of CoA to acrylate groups on the PEG. The LED was driven at a current of 700 mA which corresponds to a radiant flux of 800 mW (manufacturer's specifications) for at least 1 h.

CoA functionalized surfaces and cantilevers stored in coupling buffer (50 mM sodium phosphate pH 7.2, 50 mM NaCl, 10 mM EDTA buffer) at 8° C were stable for weeks.

When different protein constructs were compared with a single cantilever, up to 10 spatially separated spots were created using a silicone mask (CultureWell reusable gaskets, Grace Bio-Labs, Bend, OR, USA) heated to 60° C and securely pressed onto on a silanized microscope slide (76x26 mm, Carl Roth, Karlsruhe Germany). Pegylation and CoA coupling in individual wells was achieved following the protocols described above (*6*).

Both variants of the protocol resulted in cantilevers and surfaces covalently coated in PEG-CoA. Cantilevers and surfaces were again rinsed in ultrapure water. Functionalization was achieved by covalently coupling proteins via their ybbr-tag to CoA by the SFP enzyme. The proteins of interest were diluted into TBS (25 mM Tris, 150 mM NaCl, pH 7.4) supplemented with 10 mM $MgCl_2$. Cantilevers were typically incubated with 40 μM of protein of interest and 3 μM Sfp phosphopantetheinyl transferase (SFP) for 2 h. The glass surfaces were incubated with 2 – 10 μM of protein of interest 2 μM SFP for 30 - 60 min. Both samples were rinsed extensively with at least 60 mL measurement buffer (TBS: 25 mM Tris, 150 mM NaCl, pH 7.4) buffer before experiments.

AFM-SMFS

AFM-SMFS data was acquired on a custom-built AFM operated in closed loop by a MFP3D controller (Asylum Research, Santa Barbara, CA, USA) programmed in Igor Pro 6 (Wavemetrics, OR, USA). Cantilevers were briefly (<150 ms) and softly (< 200 pN) brought in contact with the functionalized surface and then retracted at constant velocities ranging from 0.4, 0.8, 1.6, 3.2 and 6.4 μm s^{-1} for a dynamic force spectrum, otherwise a velocity of 1.6 μm s^{-1} was used. Following each curve, the glass surface was moved horizontally by at least 100 nm to expose an unused surface area. Typically, 50000 - 100000 curves were recorded per experiment. When quantitative comparisons of absolute forces were required, a single cantilever was used to probe multiple spatially separated spots on the same surface, created using the protocol described above. To calibrate cantilevers the Inverse Optical Cantilever Sensitivity (InvOLS) was determined as the most probable value of typically 40 hard indentation curves. Cantilevers spring constants were calculated using the equipartition theorem method with typical spring constants between 70-150 pN nm^{-1} (*7, 8*). A full list of calibrated spring constants is provided below, as they are the stiffness of the pulling handle, which may influence the rupture forces measured.

Spring constants of cantilevers for data shown:
Figure 1D, E, G , Figure 3A, SI Figure S12C, D – SdrG:Fgß native/non-native
   $k_{Cantilever}$ = 128 pN nm^{-1}
Figure 2C, Figure S2A – SdrG:Fgß (Phenylalanine mutants)
   $k_{Cantilever}$ = 92.6 pN nm^{-1}
Figure 3B, Figure S2C – SdrG:minimized peptide
   $k_{Cantilever}$ = 95.8 pN nm^{-1}
Figure 3C – SdrG(truncated latch):Fgß
   $k_{Cantilever}$ = 75.8 pN nm^{-1}

Figure 4C – ClfB:K10
    $k_{Cantilever}$ = 144 pN nm^{-1}
Figure 4F – comparison of adhesins SdrG, ClfB, SdrE, ClfA, FnBPA, Bbp
    $k_{Cantilever}$ = 121 pN nm^{-1}
Figure S19 – ClfB:K10_GS – pure glycine-serine target
    $k_{Cantilever}$ = 153 pN nm^{-1}

SMFS data analysis

Data analysis was carried out in Python 2.7 (Python Software Foundation) (*9–11*). Laser spot drift on the cantilever relative to the calibration curve was corrected *via* the baseline noise (determined as the last 5 % of datapoints for each curve) for all curves and smoothed with a moving median. The inverse optical lever sensitivity (InvOLS) for each curve was linearly corrected relative to the InvOLS value of the calibration curve.

Raw data were transformed from photodiode and piezo voltages into physical units with the cantilever calibration values: The piezo sensitivity, the InvOLS (scaled with the drift correction) and the cantilever spring constant (k).

The last rupture peak of every curve was coarsely detected and the subsequent 15 nm of the baseline force signal were averaged and used to determine the curve baseline and set it to zero force. The origin of molecule extension was then set as the first and closest point to zero force. A correction for cantilever bending, to determine the extension value of the cantilever tip was applied. Bending was given by the forces measured and was used on all extension datapoints (x) by correcting with their corresponding force datapoint (F) as x_{corr} = x - F/k.

For peak detection, data were denoised with Total Variation Denoising (TVD, denoised data not shown in plots) (*12, 13*), and rupture events detected as significant drops in force relative to the baseline noise. A three-regime model by Livadaru et. al (*14*). was used to model the elastic behavior of contour lengths freed by unfolding events and transformed into contour length space (*15*) (Livadaru et. al. model parameters were: stiff element b = 0.11 nm and bond angle γ = 41°). A quantum mechanical correction was used to account for bond stretching at high forces (*16*). Especially at forces larger than 1 nN this correction was essential to be able to fit the data to polymer elasticity models accurately. Peaks were assigned their contour length in diagrams assembled through Kernel Density Estimates (KDE) of the contour length transformed force-extension data. The KDE bandwidth was chosen as 1 nm. The loading rate was fitted as the linear slope of force vs. time of the last 4 nm preceding a peak.

Rupture force histograms for the respective peaks and dynamic force spectra were assembled from all curves showing the ddFLN4 fingerprint. When no fingerprint unfolding was possible due to low complex rupture forces as in the case of inverted Fgß tethering, only curves with single rupture events showing clean WLC behavior were included. The most probable loading rate of all complex rupture events was determined with a KDE, with the bandwidth chosen through the Silverman estimator (*17*). This value was used to fit the unfolding or rupture force histograms with the Bell-Evans (BE) model for each pulling velocity (*18, 19*). Errors in all diagrams are given as the asymmetric full width at half maximum (FWHM) of each probability distribution. A final fit with either the Bell-Evans (BE) model (*18, 19*) or the model by Dudko, Hummer and Szabo (DHS)

(*20*) was performed through the most probable rupture forces and loading rates for each pulling velocity to determine the distance to the transition state Δx_0 and natural off-rate at zero force $k_{off,0}$, and additionally for the DHS model the energy barrier ΔG^{++} in units of $k_B T$ at T = 300 K.

Simulation Methods

The structure of the *S. epidermidis* adhesin SdrG binding to fibrinogen ß had been solved by means of X-ray crystallography at 1.86 Å resolution and was available at the protein data bank (PDB: 1R17) (*21*). The structure of *S. aureus* adhesin ClfB in complex with K10 had been solved at 2.6 Å resolution (PDB: 3ASW) (*22*). Employing advanced run options of QwikMD (*23*), the structure was solvated and the net charge of the system was neutralized using sodium counter ions. In total, approximately 240,000 atoms were simulated in each simulation. The MD simulations in the present study were performed employing the NAMD molecular dynamics package (*24*). The CHARMM36 force field (*25*), along with the TIP3 water model (*26*) was used to describe all systems. The simulations were performed assuming periodic boundary conditions in the NpT ensemble with temperature maintained at 300 K using Langevin dynamics for temperature and pressure coupling, the latter kept at 1 bar. A distance cut-off of 11.0 Å was applied to short-range non-bonded interactions, whereas long-range electrostatic interactions were treated using the particle-mesh Ewald (PME) (*27*) method. The equations of motion were integrated using the r-RESPA multiple time step scheme (*24*) to update the van der Waals interactions every step and electrostatic interactions every two steps. The time step of integration was chosen to be 2 fs for all simulations performed. Before the MD simulations all the systems were submitted to an energy minimization protocol for 1,000 steps. An MD simulation with position restraints in the protein backbone atoms was performed for 1 ns, with temperature ramping from 0k to 300 K in the first 0.5 ns, which served to pre-equilibrate the system before the steered molecular dynamics (SMD) simulations. The same protocol was also employed for all 43 SdrG system variants and ClfB system simulated in this work. All mutants or partially deleted systems were prepared using QwikMD. Systems with longer peptide were peptide chains were randomly positioned following previously assigned protocols (*28, 29*). For systems ID 41 and 42 (see Supporting Table S20), Modeller 9.18 (*30, 31*) was employed to model the unresolved C and N termini of the elongated Fgß peptide.

With structures properly equilibrated and checked, SMD simulations (*18*) were performed using a constant velocity stretching (SMD-CV protocol), employing ten different pulling speeds: 250, 125, 50, 25, 12.5, 2.5, 1.25, 0.5, 0.25 and 0.05 Å/ns. Replicas were performed for many of the system variants (see Supporting Table X) using the 2.5 Å/ns pulling speed for 20 ns. For the Fgß WT system, replicas were also performed at 250 and 25 Å/ns pulling speed in order to produce a dynamic force spectrum, presented in Fig. S3. Simulations with multiple pulling speeds (250, 125, 25, 12.5, 2.5, and 0.25 Å/ns) were also performed for the system with elongated Fgß peptide in order to produce the dynamic force spectrum presented in Fig. 1G. In total, almost 50 μs of production SMD were performed using nearly 30 million processor-hours of GPU accelerated XK nodes of the NCSA/Blue Waters supercomputer. SMD was employed by harmonically restraining the position of an amino acid residue, and moving a second restraint point at another amino acid, with constant velocity in the z axis (simulations

6

were performed in both +z and –z directions). The procedure is equivalent to attaching one end of a harmonic spring to the end of a domain and pulling on the end of the other domain with another spring. The force applied to the harmonic spring is then monitored during the time of the molecular dynamics simulation. The pulling point was moved with constant velocity along the z-axis and due to the single anchoring point and the single pulling point the system is quickly aligned along the z-axis. Owing to the flexibility of the linkers between the domains of interest and the fingerprint domains, this approach reproduces the experimental set-up.

The pulling speeds employed in our steered MD simulations make the difference in the force loading rate between experiment and simulation in the range of 10^6 pN/s. It is important to note that the slope in the dynamic force spectrum (Fig. 1G, S3) can change with increasing pulling speeds, resulting in a nonlinear upturn at higher pulling velocities as shown by Rico et al. (*32*). This effect is caused by a shift from a stochastic to a deterministic unfolding regime. In the former, the unfolding process is governed by spontaneous, thermal unfolding under a given force, while in the latter, the high pulling velocities leave the protein insufficient time to sample its energy landscape. As described in the Dudko, Hummer and Szabo model (DHS model, (*20*)), the regime transition can happen at different loading rates and is characterized by the critical force $F_c=\Delta G/(v\ \Delta x)$, which here computes to values larger than 4400 pN, depending on the individual fit. Therefore, the transition from stochastic to deterministic regime strongly depends on the general mechanical stability of the system under investigation. The high stability of the investigated systems suggests that our SMD simulations were carried out at loading rates where unfolding is still dominated by stochastic fluctuations, allowing us for an accurate description of the system in this study.

Simulation Data Analysis

Simulation force-time traces were analyzed analogously to experimental data. For each simulation, the rupture force was determined as the highest force of a trace and the force loading rate was determined as a linear fit to the force-vs time traces immediately before rupture. Analyses of MD trajectories were carried out employing VMD (*33*) and its plug-ins, except for the contact surface between the peptide and the adhesin protein, which was calculated using PyContact (*34*). In VMD, the Network View plugin (*35*) was employed to perform a force propagation pathway analysis, following the same protocol previously established by our groups (*36*). A network was defined as a set of nodes, all α-carbons, with connecting edges. The dynamical networks were constructed from 2 ns windows in the force ramp near the highest force regime.

Protein and peptide sequences and structures

SD-repeat protein G – SdrG (*Staphylococcus epidermidis*, Uniprot Q9KI13, PDB 1R17):
N2domain_N3domain
EQGSNVNHLIKVTDQSITEGYDDSDGIIKAHDAENLIYDVTFEVDDKVKSGDTMTVNIDKNT
VPSDLTDSFAIPKIKDNSGEIIATGTYDNTNKQITYTFTDYVDKYENIKAHLKLTSYIDKSK
VPNNNTKLDVEYKTALSSVNKTITVEY

```
QKPNENRTANLQSMFTNIDTKNHTVEQTIYINPLRYSAKETNVNISGNGDEGSTIIDDSTII
KVYKVGDNQNLPDSNRIYDYSEYEDVTNDDYAQLGNNNDVNINFGNIDSPYIIKVISKYDPN
KDDYTTIQQTVTMQTTINEYTGEFRTASYDNTIAFSTSSGQGQGDLPPE
```

Fgß (from the N-termial region of mature human fibrinogen ß-chain Uniprot P02675)
```
NEEGFFSARGHRPLD
```

Clumping factor B – ClfB (from *Staphylococcus aureus*, Uniprot Q6GDH2, PDB 3ASW): N2domain_N3domain
```
PVVNAADAKGTNVNDKVTASNFKLEKTTFDPNQSGNTFMAANFTVTDKVKSGDYFTAKLPDS
LTGNGDVDYSNSNNTMPIADIKSTNGDVVAKATYDILTKTYTFVFTDYVNNKENINGQFSLP
LFTDRAKAPKSGTYDANINIADEMFNNKITYNYSSPIAGIDKPNGANIS
SQIIGVDTASGQNTYKQTVFVNPKQRVLGNTWVYIKGYQDKIEESSGKVSATDTKLRIFEVN
DTSKLSDSYYADPNDSNLKEVTDQFKNRIYYEHPNVASIKFGDITKTYVVLVEGHYDNTGKN
LKTQVIQENVDPVTNRDYSIFGWNNENVVRYGGGSADGDSAV
```

K10 (from the C-terminal region of human Keratin 10, Uniprot P13645)
```
YGGGSSGGGSSGGGH
```

SD-repeat protein E – SdrE (from *Staphylococcus aureus*, Uniprot Q932F7 (crystal structure) or Q2FJ77 (exact sequence), PDB 5WTB): N2domain_N3domain
```
AVAQPAAVASNNVNDLIKVTKQTIKVGDGKDNVAAAHDGKDIEYDTEFTIDNKVKKGDTMTI
NYDKNVIPSDLTDKNDPIDITDPSGEVIAKGTFDKATKQITYTFTDYVDKYEDIKSRLTLYS
YIDKKTVPNETSLNLTFATAGKETSQNVTVDYQDPMVHGDSNIQSIFTKLDEDKQTIEQQIY
VNPLKKSATNTKVDIAGSQVDDYGNIKLGNGSTIIDQNTEIKVYKVNSDQQLPQSNRIYDFS
QYEDVTSQFDNKKSFSNNVATLDFGDINSAYIIKVVSKYTPTSDGELDIAQGTSMRTTDKYG
YYNYAGYSNFIVTSNDTGGGDGTVKPEEK
```

Clumping factor A – ClfA (from *Staphylococcus aureus*, Uniprot: Q2G015, PDB 2VR3): N2domain_N3domain
```
APVAGTDITNQLTNVTVGIDSGTTVYPHQAGYVKLNYGFSVPNSAVKGDTFKITVPKELNLN
GVTSTAKVPPIMAGDQVLANGVIDSDGNVIYFTDYVNTKDDVKATLTMPAYIDPENVKKTG
NVTLATGIGSTTANKTVLVDYEKYGKFYNLSIKGTIDQIDKTNNTYRQTIYVNPSGDNVIAP
VLTGNLKPNTDSNALIDQQNTSIKVYKVDNAADLSESYFVNPENFEDVTNSVNITFPNPNQY
KVEFNTPDDQITTPYIVVVNGHIDPNSKGDLALRSTLYGYNSNIIWRSMSWDNEVAFNNGSG
SGDGIDKPVVPEQP
```

Fibronectin-binding protein A – FnBPA (from *Staphylococcus aureus*, Uniprot P14738, PDB 4B60): N2domain_N3domain
```
SNAKVETGTDVTSKVTVEIGSIEGHNNTNKVEPHAGQRAVLKYKLKFENGLHQGDYFDFTLS
NNVNTHGVSTARKVPEIKNGSVVMATGEVLEGGKIRYTFTNDIEDKVDVTAELEINLFIDPK
TVQTNGNQTITSTLNEEQTSKELDVKYKDGIGNYYANLNGSIETFNKANNRFSHVAFIKPNN
GKTTSVTVTGTLMKGSNQNGNQPKVRIFEYLGNNEDIAKSVYANTTDTSKFKEVTSNMSGNL
NLQNNGSYSLNIENLDKTYVVHYDGEYLNGTDEVDFRTQMVGHPEQLYKYYYDRGYTLTWDN
GLVLYSNKANGNEKNGPI
```

Bone sialoprotein binding protein – Bbp (from *Staphylococcus aureus*, Uniprot: Q14U76, PDB 5CFA): N2domain_N3domain

```
ASNNVNDLITVTKQMITEGIKDDGVIQAHDGEHIIYTSDFKIDNAVKAGDTMTVKYDKHTIP
SDITDDFTPVDITDPSGEVIAKGTFDLNTKTITYKFTDYVDRYENVNAKLELNSYIDKKEVP
NETNLNLTFATADKETSKNVKVEYQKPIVKDESNIQSIFSHLDTTKHEVEQTIYVNPLKLNA
KNTNVTIKSGGVADNGDYYTGDGSTIIDSNTEIKVYKVASGQQLPQSNKIYDYSQYEDVTNS
VTINKNYGTNMANINFGDIDSAYIVKVVSKYTPGAEDDLAVQQGVRMTTTNKYNYSSYAGYT
NTILSTTDSGGGDGTVKPEEK
```

CFH (from human complement factor H, Uniprot P08603):

```
RLSSRSHTLRTTCWDGKLEYP
```

Fgγ (from human fibrinogen gamma isoform gamma-A, Uniprot: P02679-2):

```
GEGQQHHLGGAKQAGDV
```

DK (from human dermokine 10, Uniprot Q6E0U4)

```
QSGSSGSGSNGD
```

Fgα (from human fibrinogen alpha, Uniprot P02671):

```
SKQFTSSTSYNRGDS
```

Full protein construct sequences

    All sequences contain a 6xHIS (HHHHHH) tag for purification and a ybbr-tag (DSLEFIASKLA) for covalent surface anchoring. Sequences may contain a HRV 3C Protease cleavage site (LEVLFQGP) or a sortase motif (LPETGG), which were not used in this study. The wild-type ddFLN4 fingerprint contains a cysteine that has been mutated as C18S to avoid a potential cross-reaction to Maleimides.

SdrG (N2_N3 domains) – 6xHIS – ybbr

```
MGTEQGSNVNHLIKVTDQSITEGYDDSDGIIKAHDAENLIYDVTFEVDDKVKSGDTMTVNID
KNTVPSDLTDSFAIPKIKDNSGEIIATGTYDNTNKQITYTFTDYVDKYENIKAHLKLTSYID
KSKVPNNNTKLDVEYKTALSSVNKTITVEYQKPNENRTANLQSMFTNIDTKNHTVEQTIYIN
PLRYSAKETNVNISGNGDEGSTIIDDSTIIKVYKVGDNQNLPDSNRIYDYSEYEDVTNDDYA
QLGNNNDVNINFGNIDSPYIIKVISKYDPNKDDYTTIQQTVTMQTTINEYTGEFRTASYDNT
IAFSTSSGQGQGDLPPEKT
ELKLPRSRHHHHHHGSLEVLFQGPDSLEFIASKLA
```

SdrG (N2_N3 domains, truncated locking strand) – 6xHIS – ybbr

```
MGTEQGSNVNHLIKVTDQSITEGYDDSDGIIKAHDAENLIYDVTFEVDDKVKSGDTMTVNID
KNTVPSDLTDSFAIPKIKDNSGEIIATGTYDNTNKQITYTFTDYVDKYENIKAHLKLTSYID
KSKVPNNNTKLDVEYKTALSSVNKTITVEYQKPNENRTANLQSMFTNIDTKNHTVEQTIYIN
PLRYSAKETNVNISGNGDEGSTIIDDSTIIKVYKVGDNQNLPDSNRIYDYSEYEDVTNDDYA
QLGNNNDVNINFGNIDSPYIIKVISKYDPNKDDYTTIQQTVTMQTTINEYTGEFRTASYDNT
IAFSTSSGQG
ASGTGTAELKLPRSRHHHHHHGSLEVLFQGPDSLEFIASKLA
```

SdrG (N2_N3 domains deleted locking strand) – 6xHIS – ybbr

MGTEQGSNVNHLIKVTDQSITEGYDDSDGIIKAHDAENLIYDVTFEVDDKVKSGDTMTVNID
KNTVPSDLTDSFAIPKIKDNSGEIIATGTYDNTNKQITYTFTDYVDKYENIKAHLKLTSYID
KSKVPNNNTKLDVEYKTALSSVNKTITVEYQKPNENRTANLQSMFTNIDTKNHTVEQTIYIN
PLRYSAKETNVNISGNGDEGSTIIDDSTIIKVYKVGDNQNLPDSNRIYDYSEYEDVTNDDYA
QLGNNNDVNINFGNIDSPYIIKVISKYDPNKDDYTTIQQTVTMQTTINEYTGEFRTASYDNT
GASGTGTAELKLPRSRHHHHHHGSLEVLFQGPDSLEFIASKLA

Fgß – linker – ddFLN4(C18S) – 6xHIS – ybbr
WT peptide

MGTNEEGFFSARGHRPLDGSGSGSGSAGTGSGADPEKSYAEGPGLDGGESFQPSKFKIHAVD
PDGVHRTDGGDGFVVTIEGPAPVDPVMVDNGDGTYDVEFEPKEAGDYVINLTLDGDNVNGFP
KTVTVKPAPSGHHHHHHGSDSLEFIASKLA

FgßF0 – linker – ddFLN4(C18S) – 6xHIS – ybbr

MGTNEEGAASARGHRPLDGSGSGSGSAGTGSGADPEKSYAEGPGLDGGESFQPSKFKIHAVD
PDGVHRTDGGDGFVVTIEGPAPVDPVMVDNGDGTYDVEFEPKEAGDYVINLTLDGDNVNGFP
KTVTVKPAPSGHHHHHHGSDSLEFIASKLA

FgßF1 – linker – ddFLN4(C18S) – 6xHIS – ybbr

MGTNEEGAFSARGHRPLDGSGSGSGSAGTGSGADPEKSYAEGPGLDGGESFQPSKFKIHAVD
PDGVHRTDGGDGFVVTIEGPAPVDPVMVDNGDGTYDVEFEPKEAGDYVINLTLDGDNVNGFP
KTVTVKPAPSGHHHHHHGSDSLEFIASKLA

FgßF3 – linker – ddFLN4(C18S) – 6xHIS – ybbr

MGTNEEGFFFSARGHRPLDGSGSGSGSAGTGSGADPEKSYAEGPGLDGGESFQPSKFKIHAV
DPDGVHRTDGGDGFVVTIEGPAPVDPVMVDNGDGTYDVEFEPKEAGDYVINLTLDGDNVNGF
PKTVTVKPAPSGHHHHHHGSDSLEFIASKLA

FgßF- – linker – ddFLN4(C18S) – 6xHIS – ybbr
Similar to FgßF0, but phenylalanines are deleted and not replaced by alanines, see Fig S5

MGTSARGHRPLDGSGSGSGSAGTGSGADPEKSYAEGPGLDGGESFQPSKFKIHAVDPDGVHR
TDGGDGFVVTIEGPAPVDPVMVDNGDGTYDVEFEPKEAGDYVINLTLDGDNVNGFPKTVTVK
PAPSGHHHHHHGSDSLEFIASKLA

4GS – linker – ddFLN4(C18S) – 6xHIS – ybbr
negative control construct (no interacting peptide present)

MGTGSGSGSGSAGTGSGADPEKSYAEGPGLDGGESFQPSKFKIHAVDPDGVHRTDGGDGFVV
TIEGPAPVDPVMVDNGDGTYDVEFEPKEAGDYVINLTLDGDNVNGFPKTVTVKPAPSG
HHHHHHGSDSLEFIASKLA

FFSARG – linker – ddFLN4(C18S) – 6xHIS – ybbr
minimum peptide construct

MGTFFSARGGSGSGSGSAGTGSGADPEKSYAEGPGLDGGESFQPSKFKIHAVDPDGVHRTDG
GDGFVVTIEGPAPVDPVMVDNGDGTYDVEFEPKEAGDYVINLTLDGDNVNGFPKTVTVKPAP
SGHHHHHHGSDSLEFIASKLA

ClfB (N2_N3 domains) – 6xHIS – ybbr

MGTPVVNAADAKGTNVNDKVTASNFKLEKTTFDPNQSGNTFMAANFTVTDKVKSGDYFTAKL
PDSLTGNGDVDYSNSNNTMPIADIKSTNGDVVAKATYDILTKTYTFVFTDYVNNKENINGQF
SLPLFTDRAKAPKSGTYDANINIADEMFNNKITYNYSSPIAGIDKPNGANISSQIIGVDTAS
GQNTYKQTVFVNPKQRVLGNTWVYIKGYQDKIEESSGKVSATDTKLRIFEVNDTSKLSDSYY
ADPNDSNLKEVTDQFKNRIYYEHPNVASIKFGDITKTYVVLVEGHYDNTGKNLKTQVIQENV
DPVTNRDYSIFGWNNENVVRYGGGSADGDSAV
ELKLPRSRHHHHHHGSLEVLFQGPDSLEFIASKLA

ybbr – 6xHIS – ddFLN4(C18S) – linker – K10

MDSLEFIASKLAHHHHHHGSADPEKSYAEGPGLDGGESFQPSKFKIHAVDPDGVHRTDGGDG
FVVTIEGPAPVDPVMVDNGDGTYDVEFEPKEAGDYVINLTLDGDNVNGFPKTVTVKPAP
GSGSGSGSYGGGSSGGGSSGGGH

ybbr – 6xHIS – ddFLN4(C18S) – linker – K10GS

Tyrosine and Histidine are deleted from K10, a purely glycine serine sequence remains

MDSLEFIASKLAHHHHHHGSADPEKSYAEGPGLDGGESFQPSKFKIHAVDPDGVHRTDGGDG
FVVTIEGPAPVDPVMVDNGDGTYDVEFEPKEAGDYVINLTLDGDNVNGFPKTVTVKPAP
GSGSGSGSGGGSSGGGSSGGG

SdrE (N2_N3 domains) – 6xHIS – ybbr

MATAVAQPAAVASNNVNDLIKVTKQTIKVGDGKDNVAAAHDGKDIEYDTEFTIDNKVKKGDT
MTINYDKNVIPSDLTDKNDPIDITDPSGEVIAKGTFDKATKQITYTFTDYVDKYEDIKSRLT
LYSYIDKKTVPNETSLNLTFATAGKETSQNVTVDYQDPMVHGDSNIQSIFTKLDEDKQTIEQ
QIYVNPLKKSATNTKVDIAGSQVDDYGNIKLGNGSTIIDQNTEIKVYKVNSDQQLPQSNRIY
DFSQYEDVTSQFDNKKSFSNNVATLDFGDINSAYIIKVVSKYTPTSDGELDIAQGTSMRTTD
KYGYYNYAGYSNFIVTSNDTGGGDGTVKPEEK
SGHHHHHHGSDSLEFIASKLASLPETGG

ClfA (N2_N3 domains) – 6xHIS – ybbr

MATAPVAGTDITNQLTNVTVGIDSGTTVYPHQAGYVKLNYGFSVPNSAVKGDTFKITVPKEL
NLNGVTSTAKVPPIMAGDQVLANGVIDSDGNVIYTFTDYVNTKDDVKATLTMPAYIDPENVK
KTGNVTLATGIGSTTANKTVLVDYEKYGKFYNLSIKGTIDQIDKTNNTYRQTIYVNPSGDNV
IAPVLTGNLKPNTDSNALIDQQNTSIKVYKVDNAADLSESYFVNPENFEDVTNSVNITFPNP
NQYKVEFNTPDDQITTPYIVVVNGHIDPNSKGDLALRSTLYGYNSNIIWRSMSWDNEVAFNN
GSGSGDGIDKPVVPEQP
SGHHHHHHGSDSLEFIASKLASLPETGG

FnBPA (N2_N3 domains) – 6xHIS – ybbr

MATSNAKVETGTDVTSKVTVEIGSIEGHNNTNKVEPHAGQRAVLKYKLKFENGLHQGDYFDF
TLSNNVNTHGVSTARKVPEIKNGSVVMATGEVLEGGKIRYTFTNDIEDKVDVTAELEINLFI
DPKTVQTNGNQTITSTLNEEQTSKELDVKYKDGIGNYYANLNGSIETFNKANNRFSHVAFIK
PNNGKTTSVTVTGTLMKGSNQNGNQPKVRIFEYLGNNEDIAKSVYANTTDTSKFKEVTSNMS
GNLNLQNNGSYSLNIENLDKTYVVHYDGEYLNGTDEVDFRTQMVGHPEQLYKYYYDRGYTLT

WDNGLVLYSNKANGNEKNGPI
SGHHHHHHGSDSLEFIASKLASLPETGG

Bbp (N2_N3 domains) – 6xHIS – ybbr

MATASNNVNDLITVTKQMITEGIKDDGVIQAHDGEHIIYTSDFKIDNAVKAGDTMTVKYDKH
TIPSDITDDFTPVDITDPSGEVIAKGTFDLNTKTITYKFTDYVDRYENVNAKLELNSYIDKK
EVPNETNLNLTFATADKETSKNVKVEYQKPIVKDESNIQSIFSHLDTTKHEVEQTIYVNPLK
LNAKNTNVTIKSGGVADNGDYYTGDGSTIIDSNTEIKVYKVASGQQLPQSNKIYDYSQYEDV
TNSVTINKNYGTNMANINFGDIDSAYIVKVVSKYTPGAEDDLAVQQGVRMTTTNKYNYSSYA
GYTNTILSTTDSGGGDGTVKPEEK
SGHHHHHHGSDSLEFIASKLASLPETGG

CFH – Fgα – Fgß – ddFLN4(C18S) – ybbr – 6xHIS – ddFLN4(C18S) – DK – Fgγ

Multi-peptide construct to compare absolute complex rupture forces for all adhesins in their native geometries using a single AFM cantilever

MATRLSSRSHTLRTTCWDGKLEYPSGASKQFTSSTSYNRGDSSGTGFFSARGHRPLDSTSG
ADPEKSYAEGPGLDGGESFQPSKFKIHAVDPDGVHRTDGGDGFVVTIEGPAPVDPVMVDNGD
GTYDVEFEPKEAGDYVINLTLDGDNVNGFPKTVTVKPAPGSAG
DSLEFIASKLAGHHHHHHGS
ADPEKSYAEGPGLDGGESFQPSKFKIHAVDPDGVHRTDGGDGFVVTIEGPAPVDPVMVDNGD
GTYDVEFEPKEAGDYVINLTLDGDNVNGFPKTVTVKPAPGAT
QSGSSGSGSNGDTASGEGQQHHLGGAKQAGDV
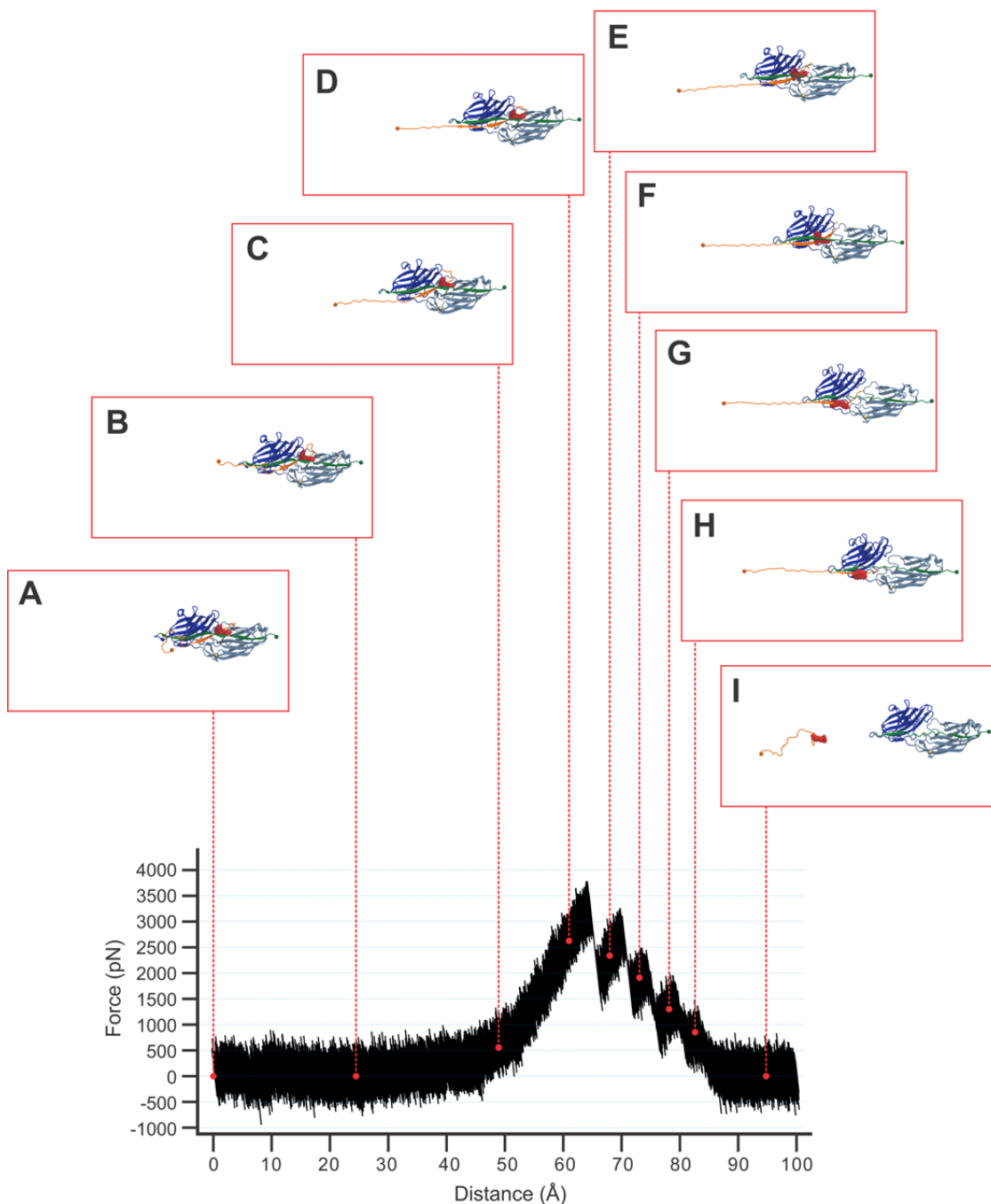
Fig. S1. SMD force-extension trace with equivalent structure snapshots.

Exemplary SMD force-extension trace in the native force propagation of SdrG (blues, locking strand in green):Fgß including experimental peptide linkers (orange, phenylalanines in red) with snapshots (A-I). The complex ruptured at almost 4000 pN. The peaks following the highest force peak correspond to other metastable geometries after slipping of the Fgß peptide to another position where the backbone-backbone H-bonds could interact again. (E-H) These were not resolved by our AFM. Metastable peaks after the main rupture event were observed in every simulation trajectory, however their number varied from one to four peaks.
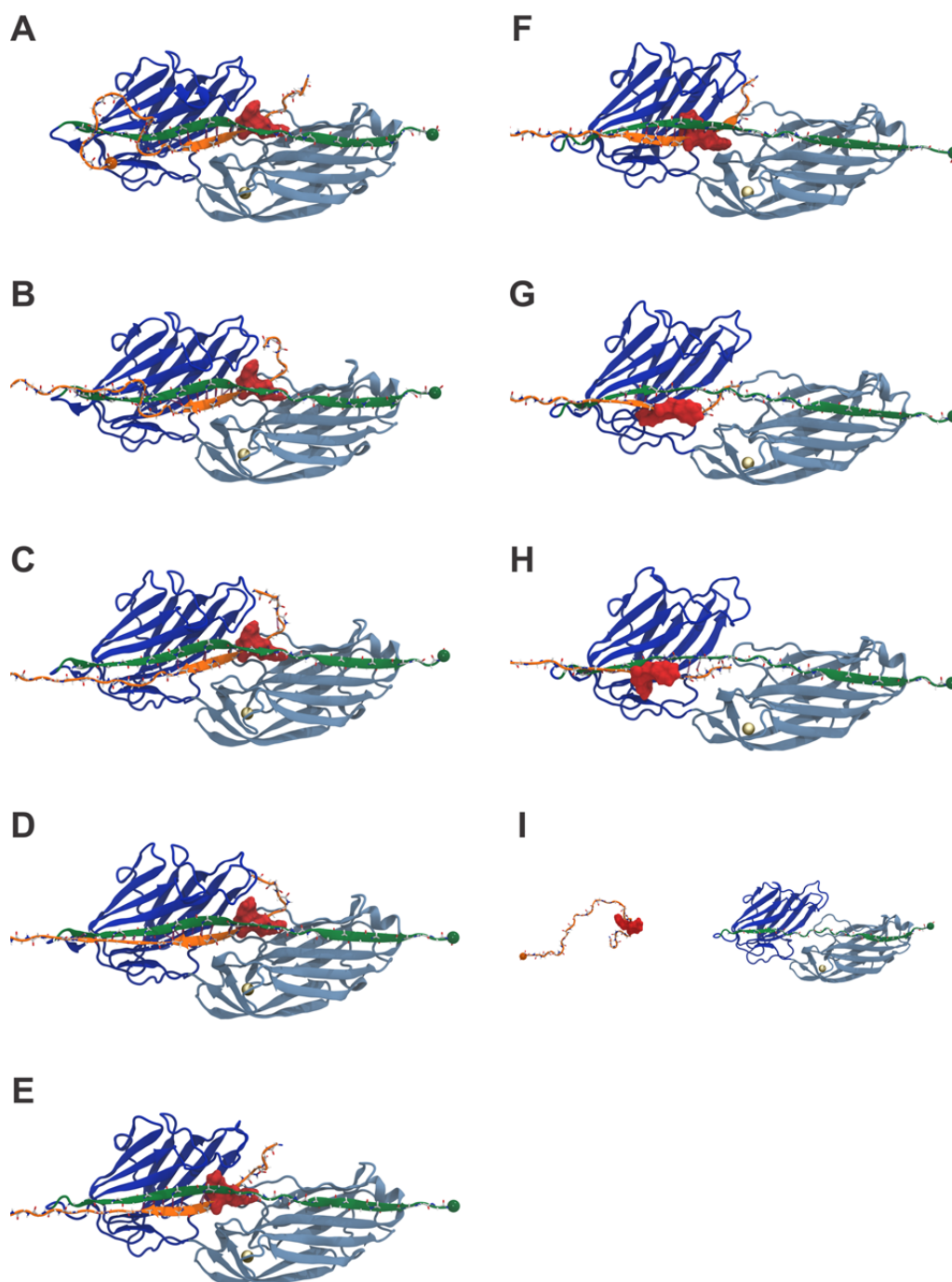
Fig. S2. Snapshots from SMD.

Representation of the evolution of SdrG (blues, locking strand in green):Fgß (orange) structure during a steered molecular dynamics simulation in the native geometry. Snapshots A-I refer to Fig. S1 steps. To help tracking the steps of the unbinding process, the bulky phenylalanine residues of the Fgß peptide are shown in red surface representation.
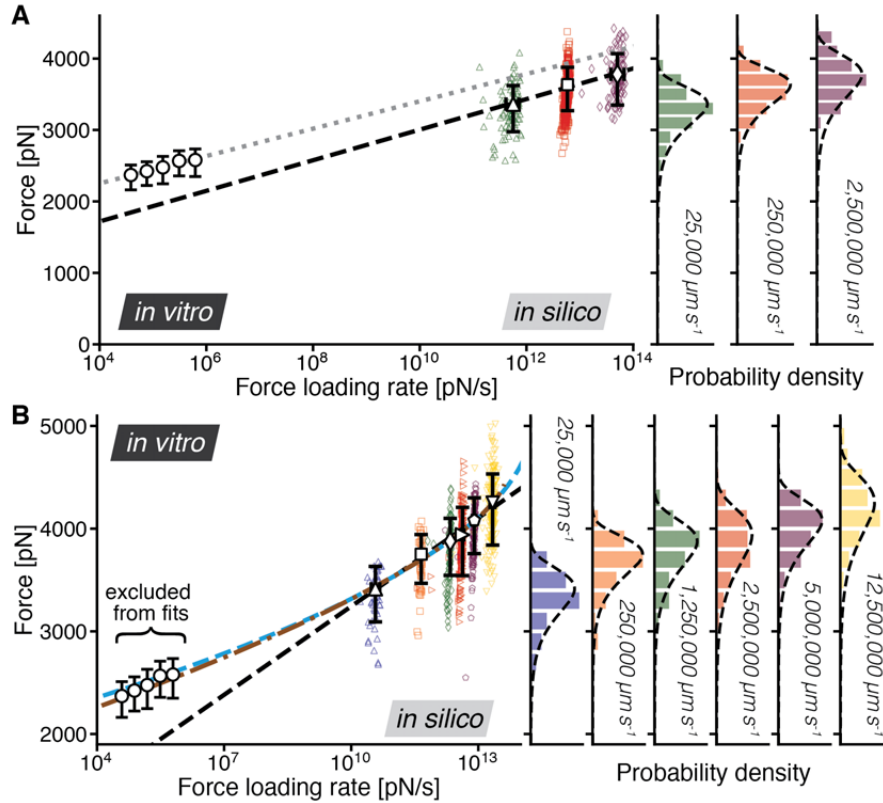
Fig. S3. Comparing dynamic force spectra for SdrG:Fgß *in vitro* and *in silico*.
(A) The experimental dynamic force spectrum from velocities of 0.4 to 6.4 μm s^{-1} for the native propagation is shown condensed as open circles (corresponding BE fit as gray dotted line). In the simulation shown we employed the Fgß WT adapted from PDB ID 1R17, in which only parts of the target sequence (namely GGFFSARGHRP) are resolved. The complete peptide investigated experimentally is 15 amino acids long and tethered by a linker (see protein sequences and Fig. S1-S2) and was presented in Fig 1G, as it corresponds exactly to the experiment. SMD simulations here cover velocities of 25,000 μm s^{-1} (green triangles, N = 100), 250,000 μm s^{-1} (red squares, N = 487), 2,500,000 μm s^{-1} (purple diamonds, N = 100) and are shown with a corresponding BE fit (black, dashed line, Δx = 0.045 nm, k_{off}^0 = 1.00E-6 s^{-1}). *In vitro* and *in silico* data agree on the general force regimes, the remaining discrepancies can be attributed to the linkers and additional amino acids missing in SMD, which resolved these differences as seen in Fig. 1G. (B) To assess the predictive power of the SMD simulations at different velocities (here from 25,000 to 12,500,000 μm/s, see Fig. 1G, N = 746) we performed a DHS and BE model fit exclusively through the SMD data. The DHS fits (cusp potential Δx = 0.14 nm, k_{off}^0 = 5.0 E-24 s^{-1}, ΔG^{++} = 83 k$_B$T, cyan dashed line and linear-cubic potential Δx = 0.089 nm, k_{off}^0 = 9.3E-17 s^{-1}, ΔG^{++} = 64 k$_B$T, brown dash-dotted line) yield a very good prediction of the experimental force results (shown as black open circles), whereas the BE fit (Δx = 0.033 nm, k_{off}^0 = 4.1E-4 s^{-1}, black dashed line) underestimates them as it does not model the slight upturn of forces at very high loading rates. In principle, SMD simulations with sufficient statistics can be used to predict the experimental force regime for this system.

15
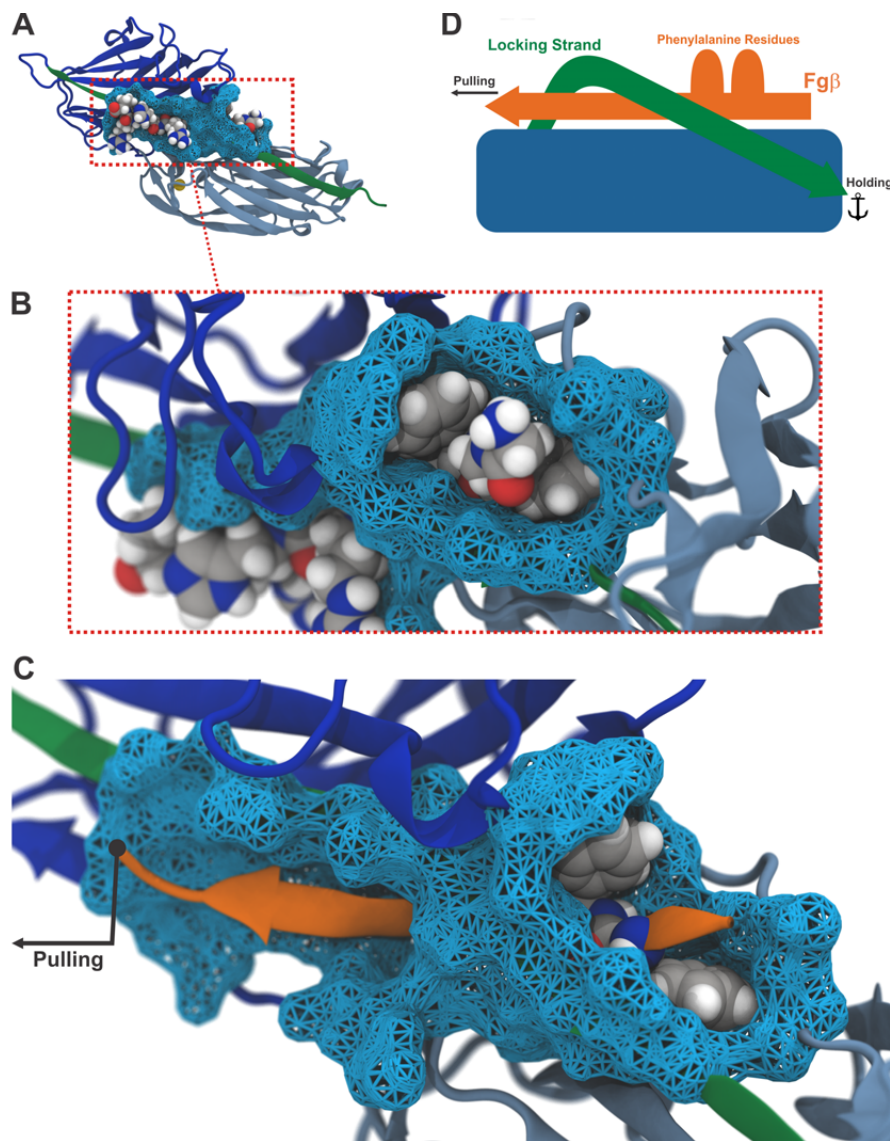
Fig. S4. The previously described "bulgy plug" has only marginal influence on the high forces.
(A) Structure of the SdrG:Fgß complex with the locking strand (green) connecting the Ig-fold N2 (light blue) and N3 (dark blue) domains. Fgß is shown in van der Waals representation, demonstrating the perfect fit in the narrow constriction region, which is shown as wire-frame cyan surface. (B) Close view of the N-terminal region of the Fgß peptide, showing the "bulgy plug" and the narrow constriction formed by the N2:N3:locking-strand interface. (C) Detailed view of the perfect arrangement of the two phenylalanine residues that form the "bulgy plug" in the WT. The bulkiness of these residues was initially thought to be responsible for the extreme force resilience of the complex. (D) Schematic view of the "bulgy plug" mechanism. As the system is force loaded the bulky residues have to move through the narrow constriction created by the locking strand to dissociate from SdrG. The conformational difficulty of this process was thought to cause the high stability of SdrG:Fgß. However, this effect has only little influence on the high force resilience of the system.
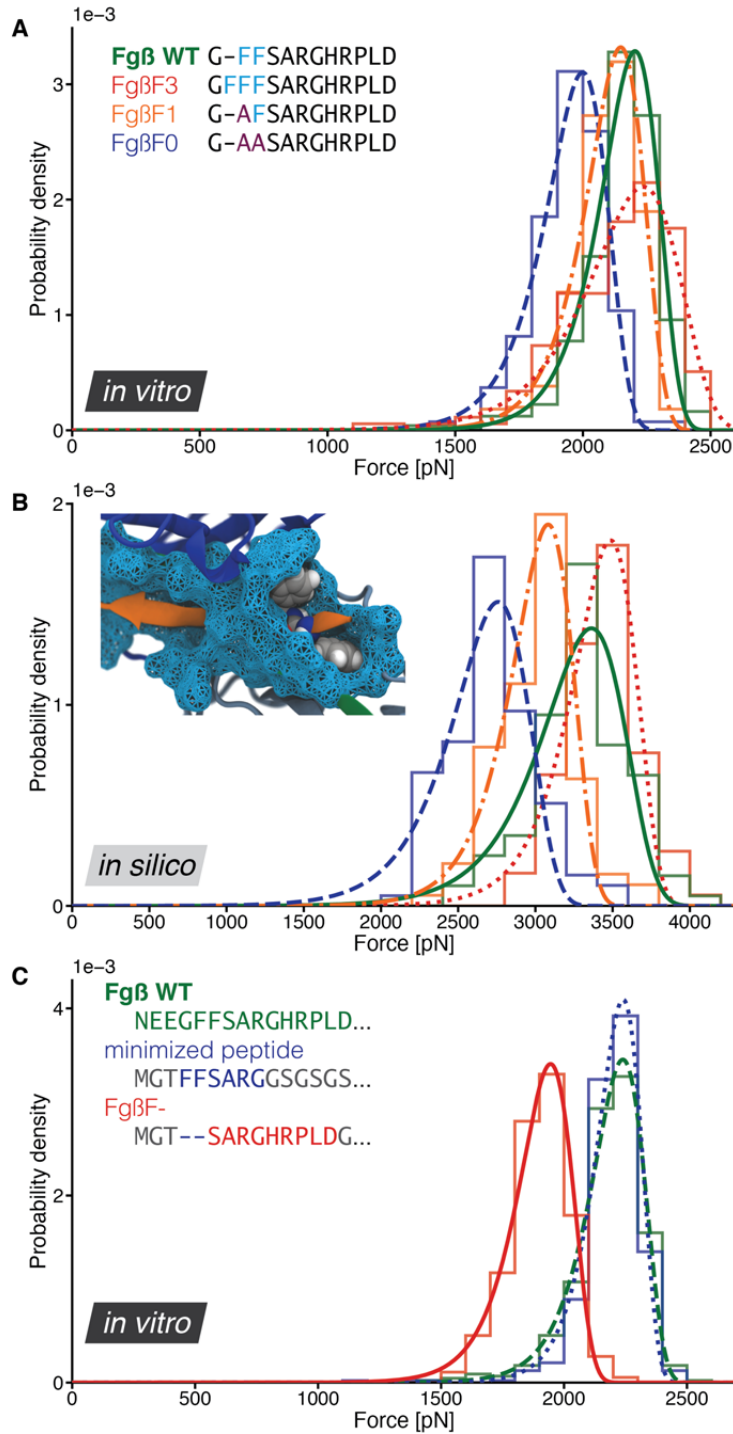
Fig. S5. Phenylalanine side chains only marginally influence SdrG:Fgß mechanostability.

(A) *In vitro* rupture force distributions recorded with a single cantilever at 1.6 μm s^{-1} retraction velocity comparing the dissociation forces of phenylalanine mutants of Fgß as histograms with lines representing the individual Bell-Evans fits. Mutant sequences are displayed: FgßF0 (blue, dashed line, N = 135), FgßF1 (orange, dash-dotted line, N =

604), WT Fgß (green, continuous line, N = 492), FgßF3 (red, dotted line, N = 178). (B) Inset showing the bulky Fgß (orange) phenylalanine sidechains as van der Waals spheres, having to move through the narrow constriction (cyan surface) created by the locking strand. Corresponding results for SMD simulations with identical assignments as in (A) for a constant velocity of 250,000 μm s^{-1} (FgßF0 N = 98, FgßF1 N = 95, Fgß N = 100, FgßF3 N = 92). The trend of weak dependence of rupture force on the number of phenylalanines in the peptide is apparent in both simulation and experiment. The FgßF0 mutant shows they are not required to achieve the regime of nN mechanostability. (C) *In vitro* rupture force distributions recorded with a single cantilever at 1.6 μm s^{-1} comparing Fgß WT (green, continuous line, N = 437) with the minimum peptide (FFSARG, embedded by start codon and linkers in gray, blue, dash-dotted line, N = 472) and FgßF-(red, dashed line, N = 179), a mutant in which the phenylalanines have been deleted instead of being replaced by alanines as in FgßF0. The rupture force distributions of minimum peptide and Fgß WT are almost indistinguishable (barely significant difference in Kolmogorov–Smirnov test, p = 0.07), thus the minimum peptide is a shorter but equally stable replacement for Fgß WT. FgßF- behaves similar to the FgßF0 mutant in (A).
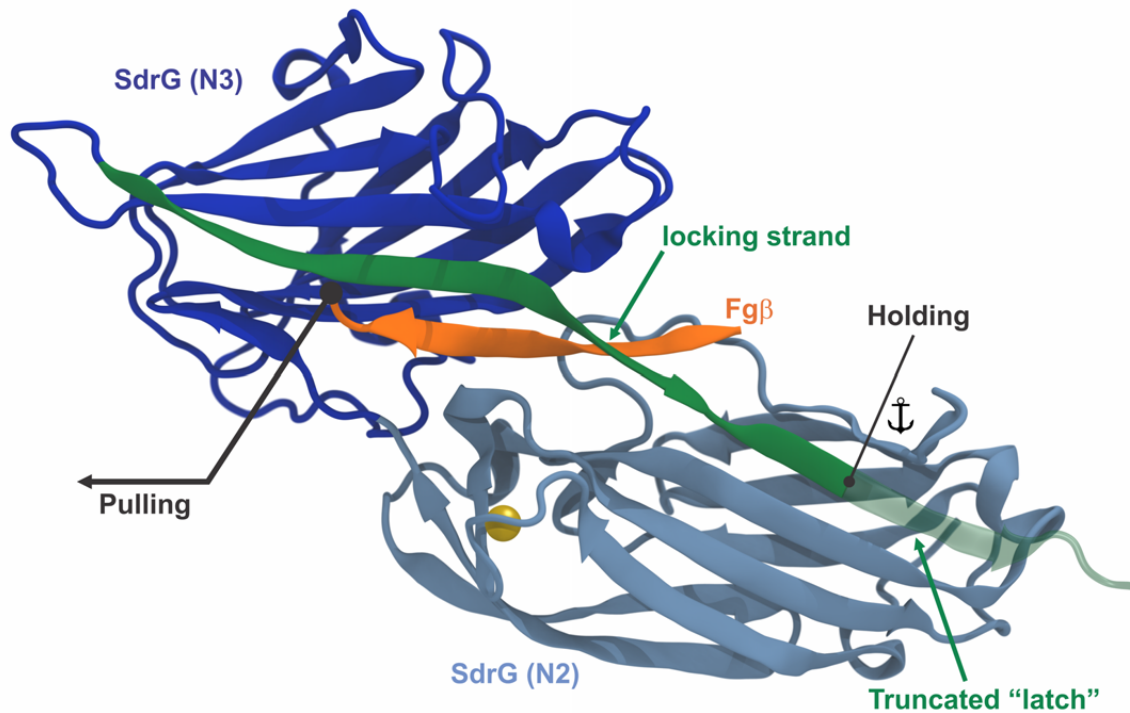
Fig. S6. Representation of SdrG:Fgß complex showing the truncated "latch".
SdrG was truncated at residue G590, which removed half of the "latch" region, here shown as translucent ß-sheet. The truncated system SdrG(274-590) was found to be mechanically indistinguishable from the WT both *in vitro* and *in silico*. Covalent isopeptide bonds between the locking strand and the N2 domain had been proposed as a possible contribution to overall SdrG stability (*37*), This hypothesis could be excluded as cause of the high forces as the SdrG truncation mutant was lacking D593, which would be a key amino acid required for the hypothesized isopeptide bond.
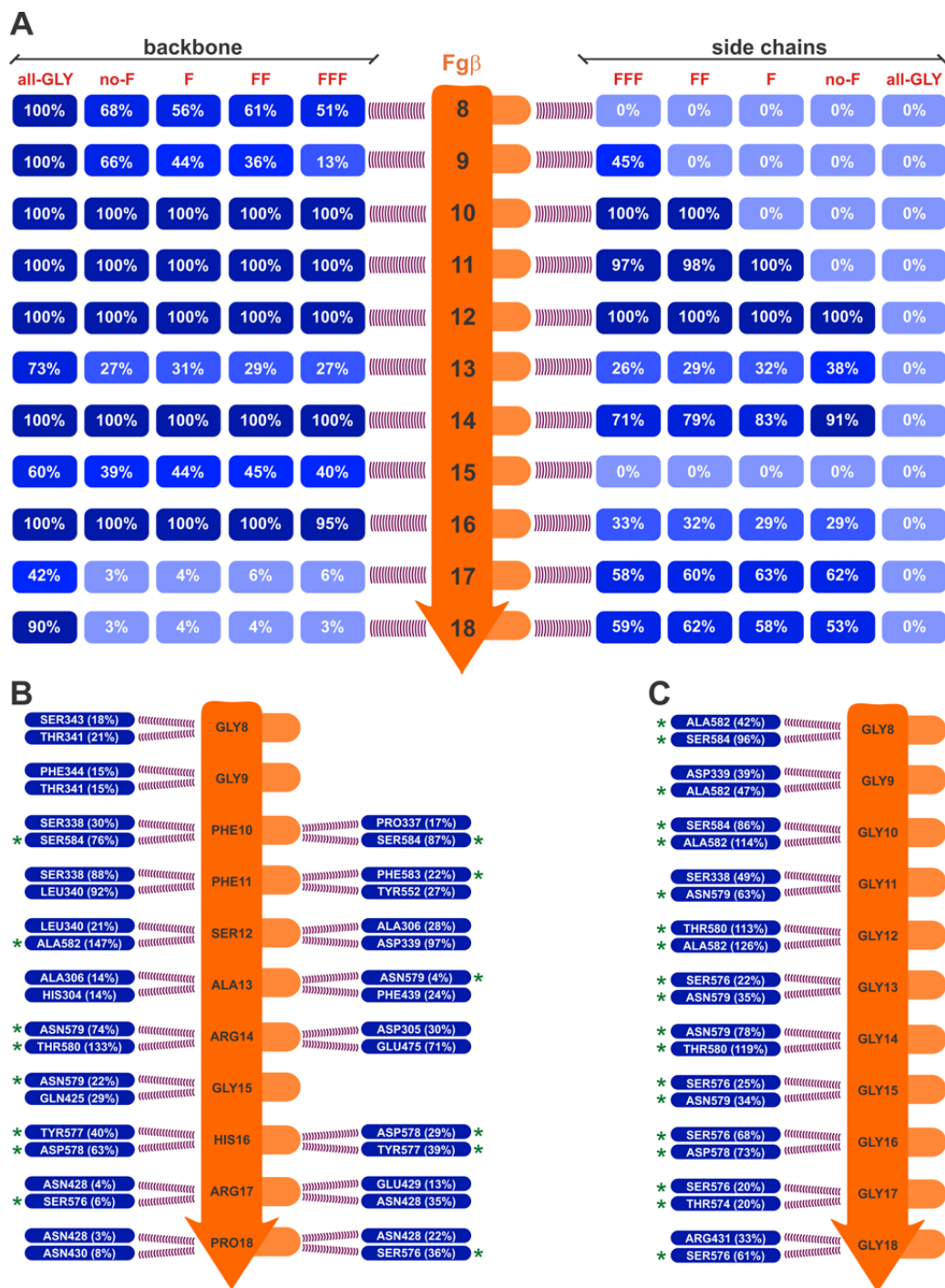
Fig. S7. Prevalence of hydrogen bonds reveals the most critical contacts between Fgß and SdrG.

A Hydrogen bond analysis for the force loaded state of SdrG:Fgß from 2 ns windows in the force ramp near the highest force regime was conducted. From all simulation replicas of a system, 2 ns long trajectories were combined to perform the hydrogen bond analysis. (A) Prevalence of hydrogen bonds between Fgß and SdrG. The matrix arrangement shows the percentage of time with at least one hydrogen bond connecting any amino acid

residue of SdrG to the Fgß backbone (left-hand side) or side chain (right-hand side). The side chains of the WT (2 phenylalanines) and the crystal structure of (FgßF3, 3 phenylalanines) have a large prevalence of hydrogen bonds. By removing these side chains (mutating to glycine) the peptide backbone becomes more flexible and it is rearranged to form more prevalent hydrogen bonds with SdrG. (B) Prevalence of hydrogen bonds between WT Fgß and SdrG. (C) Prevalence of hydrogen bonds between an all-glycine peptide and SdrG. In both (B) and (C) the prevalence can be larger than 100% as the amino acid pairs are in a geometry that would allow more than one hydrogen bond to be formed.
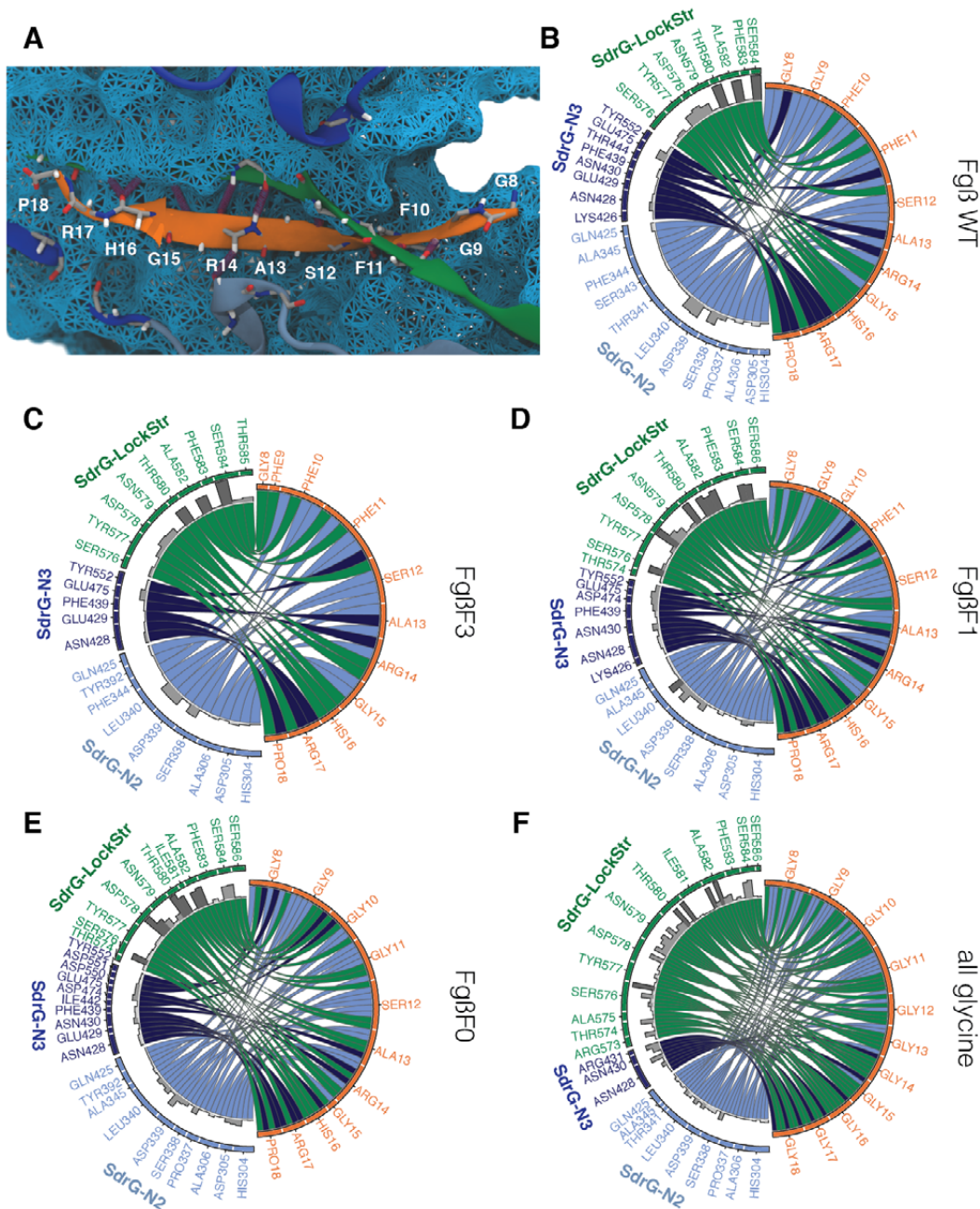
Fig. S8. Hydrogen bond contacts during SMD simulations in the high-force regime.
(A) Hydrogen bond network for WT SdrG:Fgß close up. Backbone atoms of Fgß's amino acids, as well as nearby amino acids, are shown in licorice representation. The hydrogen bonds between them are shown in purple. A partial surface of the binding cleft formed by SdrG is shown in cyan. (B – F) Hydrogen bond contact maps for the Fgß WT peptide (B), the phenylalanine mutants FgßF3/F1/F0 (C, D, E), and a pure glycine sequence (F). The histograms in the left-hand side of the circle graphics show the prevalence of these contacts. The hydrogen bond analysis was performed in the high force regime, from 2 ns windows in the force ramp near the highest force peak from all replicas.
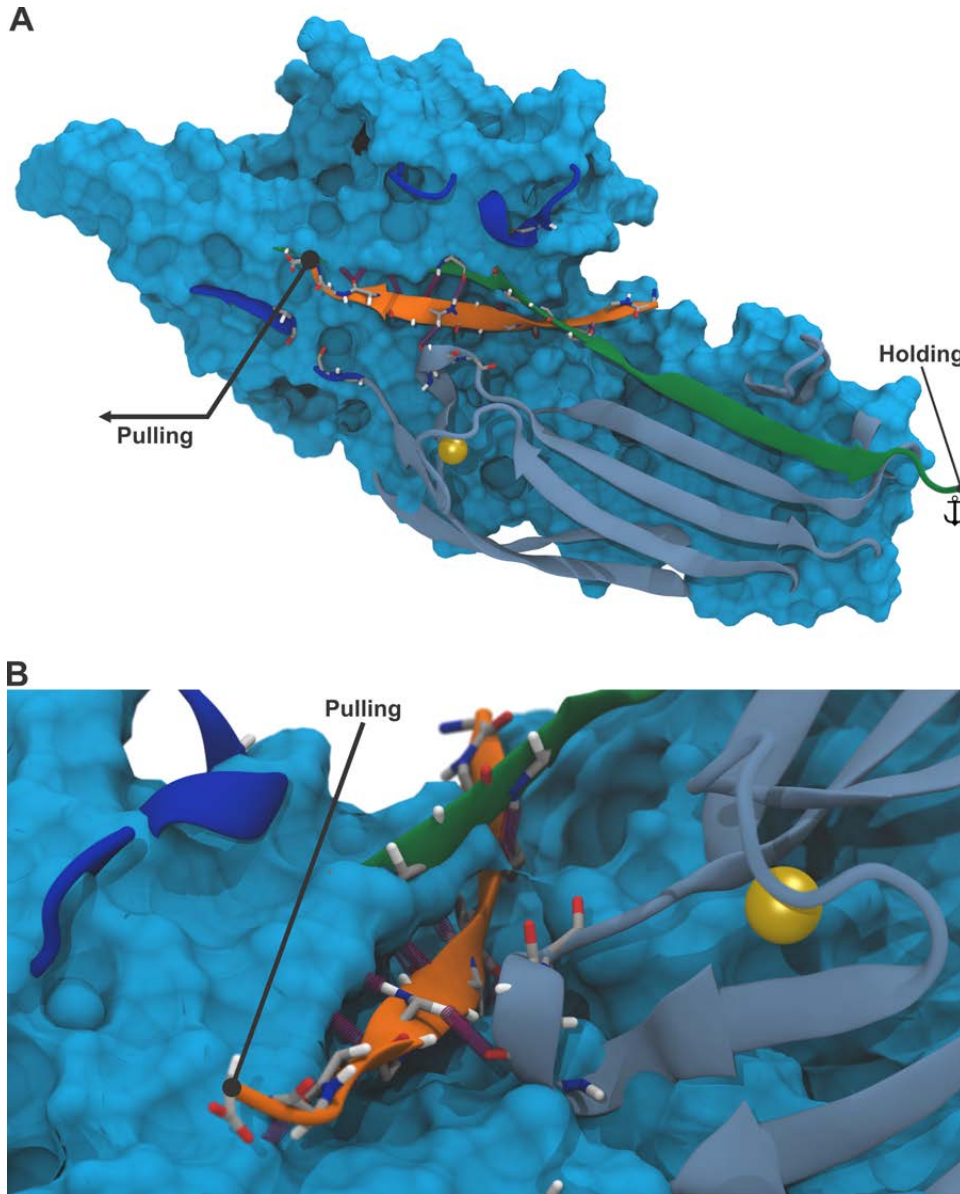
Fig. S9. The Fgß peptide is tightly confined in the binding pocket created by the locking strand.
(A) Structure of the SdrG(blue):Fgß(orange) complex with the locking strand (green) connecting the Ig-fold N2 (secondary structure representation in light blue) and N3 (secondary structure representation in dark blue). The Fgß backbone is shown in licorice representation, with hydrogen bonds (purple) connecting it to SdrG. The surface (cyan) cut shows the tight binding pocket formed by SdrG, particularly at the interface between N2 and N3 domains. (B) A closer look at the interface between SdrG and Fgß exposes the perfect confinement of the peptide in the binding pocket of SdrG. Notably, the hydrogen bonds are pointing out radially in all directions.
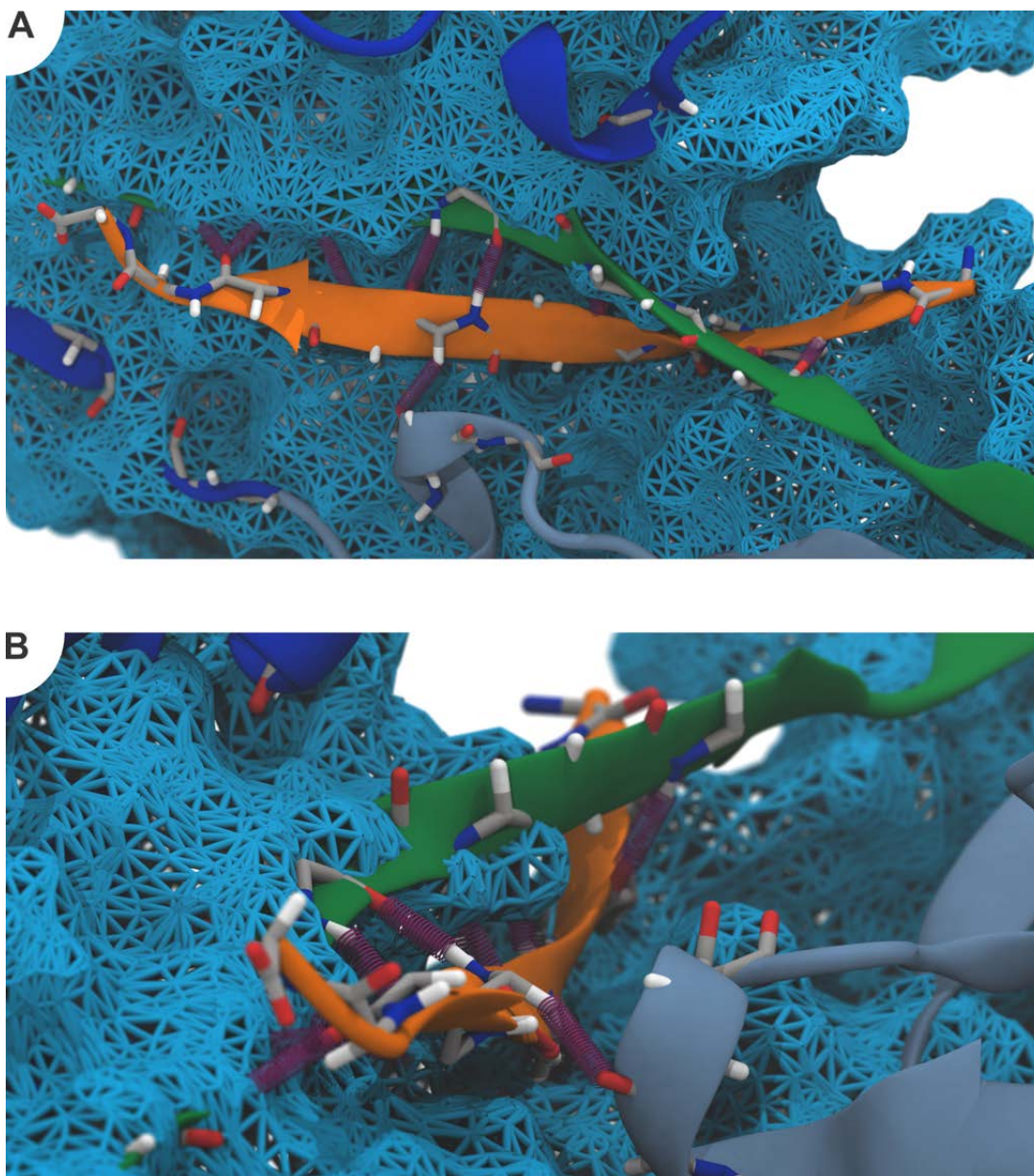
Fig. S10. Perfect confinement of the Fgß peptide by SdrG is governed by hydrogen bond interactions.

(A) Structure of the SdrG(blue):Fgß(orange) complex with the locking strand (green) connecting the Ig-fold N2 (light blue) and N3 (dark blue). The Fgß peptide backbone is shown in licorice representation, with hydrogen bonds connecting it to SdrG shown in purple. The binding pocket formed by the interface between N2 and N3 domains is partially shown as wire-frame cyan surface. The confinement created by this structure impedes peptide movement orthogonal to the force load, requiring that the backbone hydrogen bonds must all be broken cooperatively in a shear geometry. (B) A closer look at the interface between SdrG and Fgß highlights this confinement and the coiled alignment of the Fgß peptide ß-sheet (orange) and locking strand (green).
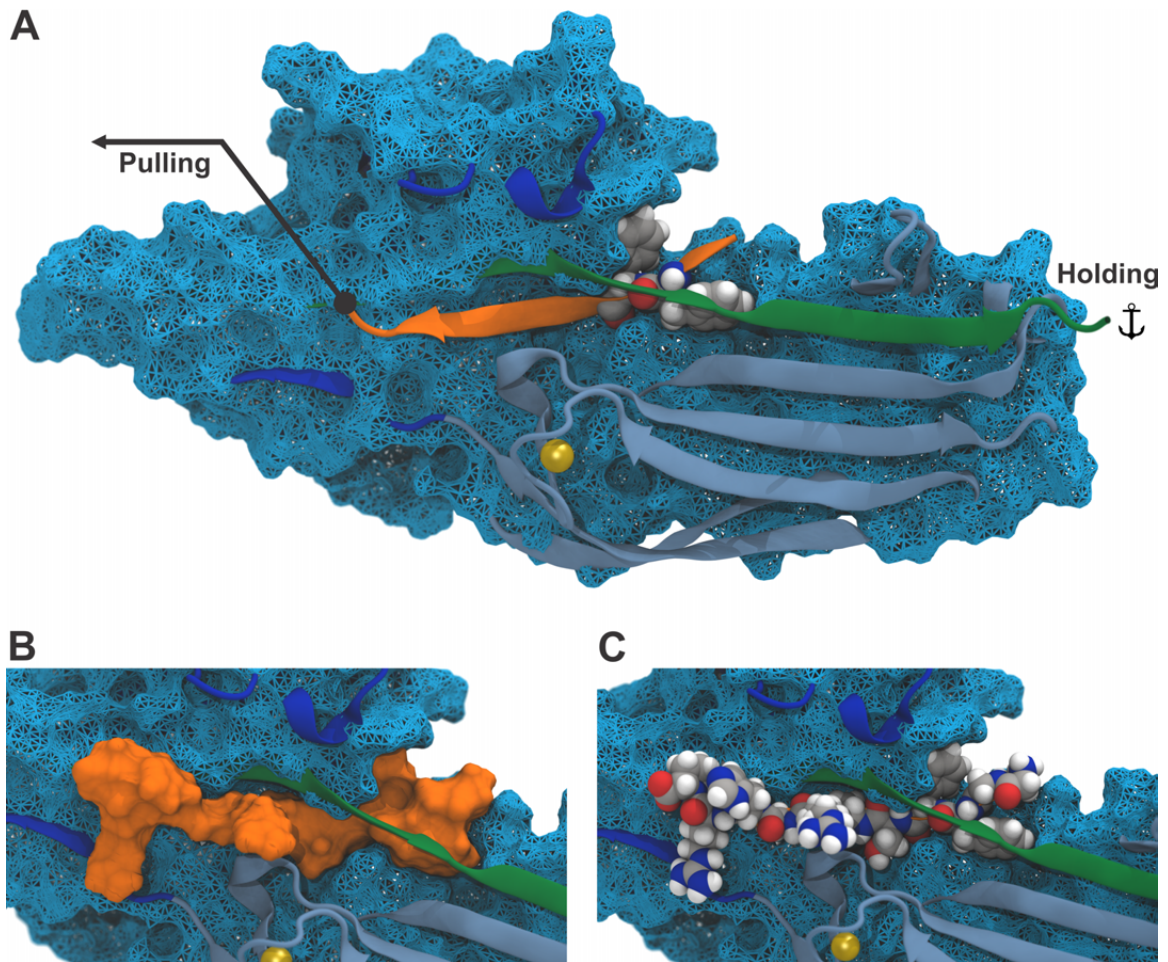
Fig. S11. Perfect confinement of the Fgß peptide within SdrG.

(A) Structure of the SdrG:Fgß complex with the locking strand (green) connecting the Ig-fold N2 (light blue) and N3 (dark blue). Fgß's phenylalanine residues are shown in van der Waals representation near the narrow constriction formed by the interface between N2 and N3 domains, which is partially shown as wire-frame cyan surface. A close look at the interface between SdrG and Fgß (orange surface) in (B) and van der Waals representation in (C) exposes the perfect confinement of the peptide in the narrow constriction region of SdrG.
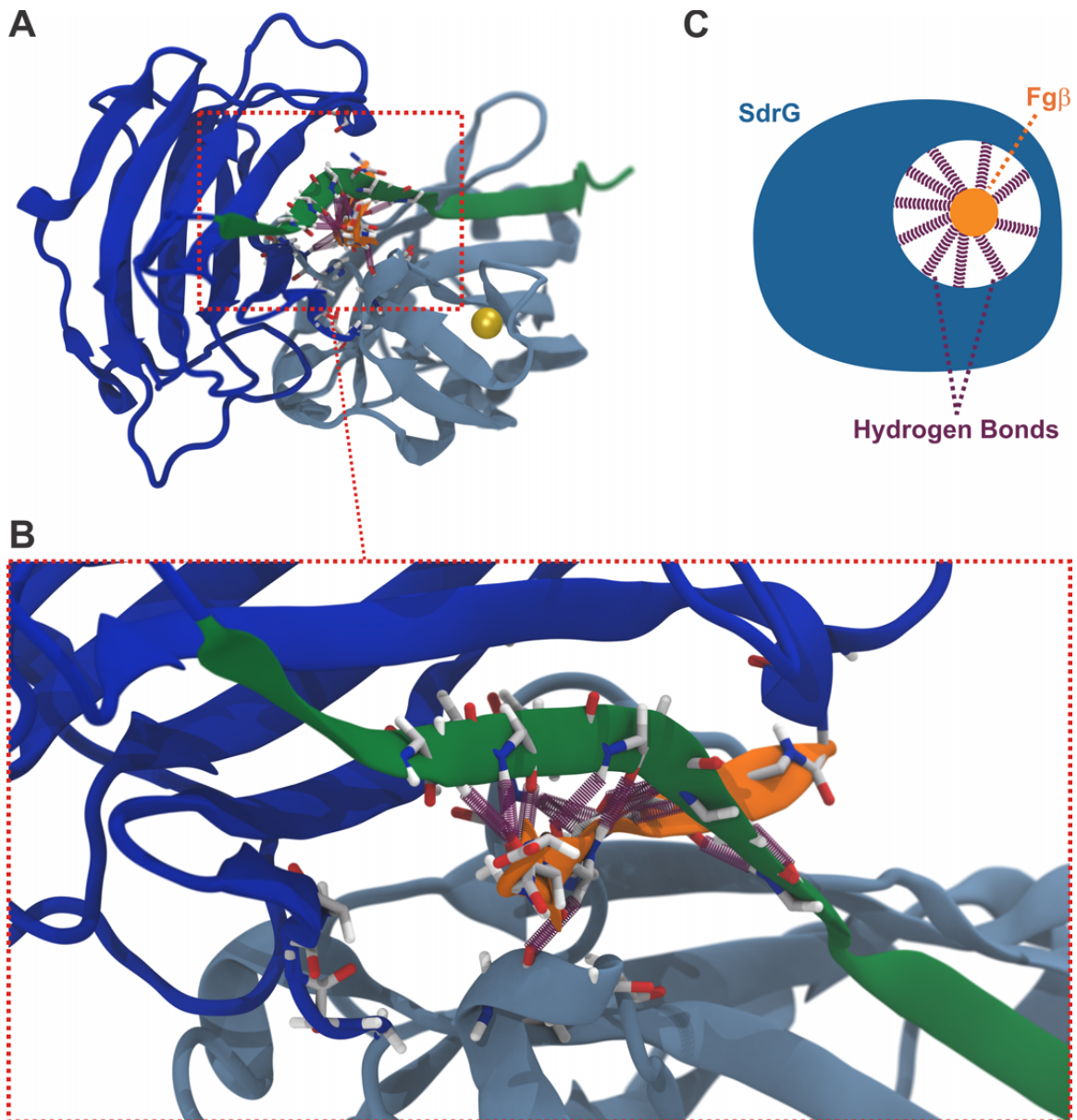
Fig. S12. The screw-like hydrogen Bond Network holds Fgß in perfect alignment.

(A) Structure of the SdrG(blue):Fgß(orange) complex with the locking strand (green) connecting the Ig-fold N2 (light blue) and N3 (dark blue) domains. Hydrogen bonds between SdrG and Fgß backbone are represented in purple, showing a screw-like arrangement, which, under force load, keeps the peptide always in the perfect shear geometry. (B) Detailed view of the screw-like arrangement of the hydrogen bonds. The Fgß backbone is kept in position by means of a hydrogen bond network, which extends in nearly all directions. (C) Schematic view of the screw-like hydrogen bond network of the SdrG:Fgß interaction.
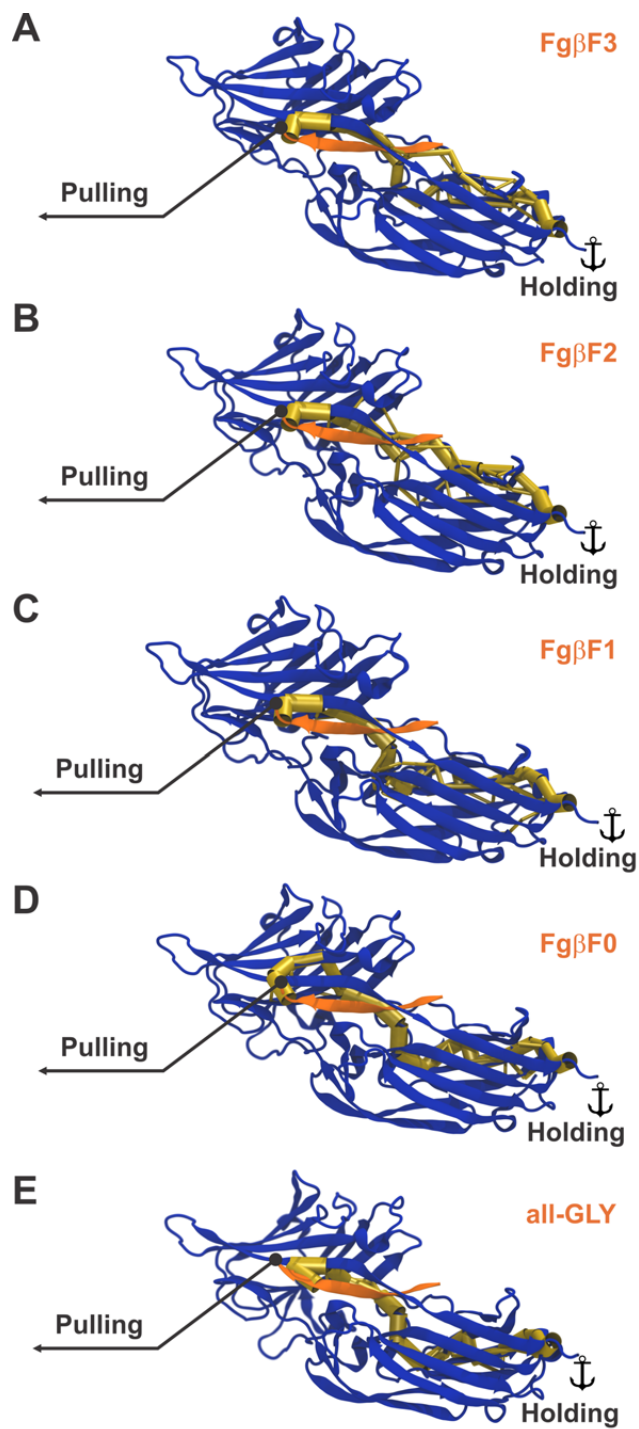
Fig. S13. Force propagation pathways.

(A-E) Force propagation pathway analysis for all systems. We used correlation-based dynamical network analysis, which calculates how an allosteric signal is transmitted between two points in a protein complex (yellow tubes) (*36*). Allostery can be understood in terms of pathways of residues that effectively transmit energy, here in the form of

mechanical stress, between different positions within a network. To calculate cross-correlation matrices, trajectories were cropped to 2 ns windows in the force ramp near the highest force regime. From all replicas, 2 ns long trajectories were combined to perform the dynamical networks analysis using VMD. It is noteworthy that the majority of the forces does not propagate through the "latch" region, which was also illustrated by the truncated latch mutant, which produced complex rupture forces almost indistinguishable from WT SdrG. This implicates that a different holding point in the N2 domain, near the locking strand C-terminus, in the force propagation pathway should also allow for high forces. This force loading configuration was tested and confirmed to produce high forces *in silico* for K379 as a holding point in SdrG. These results motivate further investigation of this configuration both *in vitro* and *in silico*.
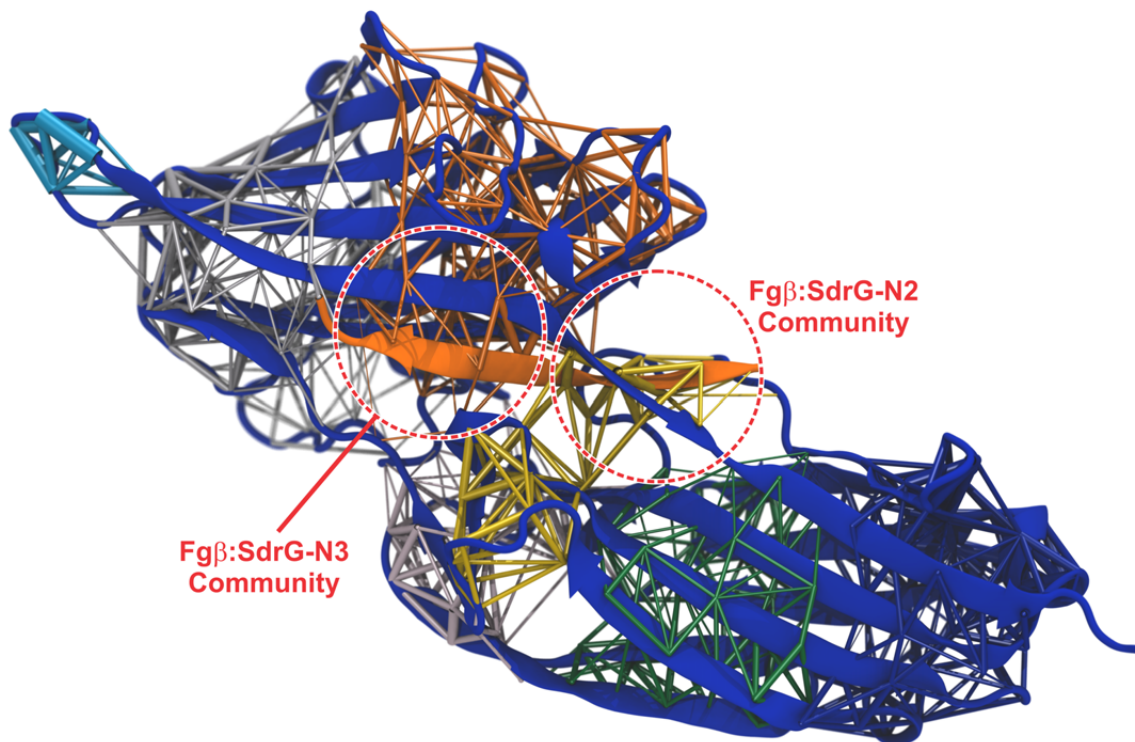
Fig. S14. Community analysis reveals the intricate network that holds N2 and N3 domains and the locking strand together with the Fgß peptide.

Network-based community analysis calculated using generalized correlation in the high force regime. For WT Fgß, trajectories were cropped to 2 ns windows in the force ramp near the highest force regime. From all 101 replicas, 2 ns long trajectories were combined to perform the community analysis, calculated using VMD. Different colors for the different communities were assigned randomly. The thickness of the network scaffold connections represents the log of the normalized correlation value. Therefore, thick connections represent highly correlated regions. The C-terminal half of the Fgß peptide (orange) is in a community with the N3 domain, whereas the N-terminal half is in a community with the N2 domain (see red circles).
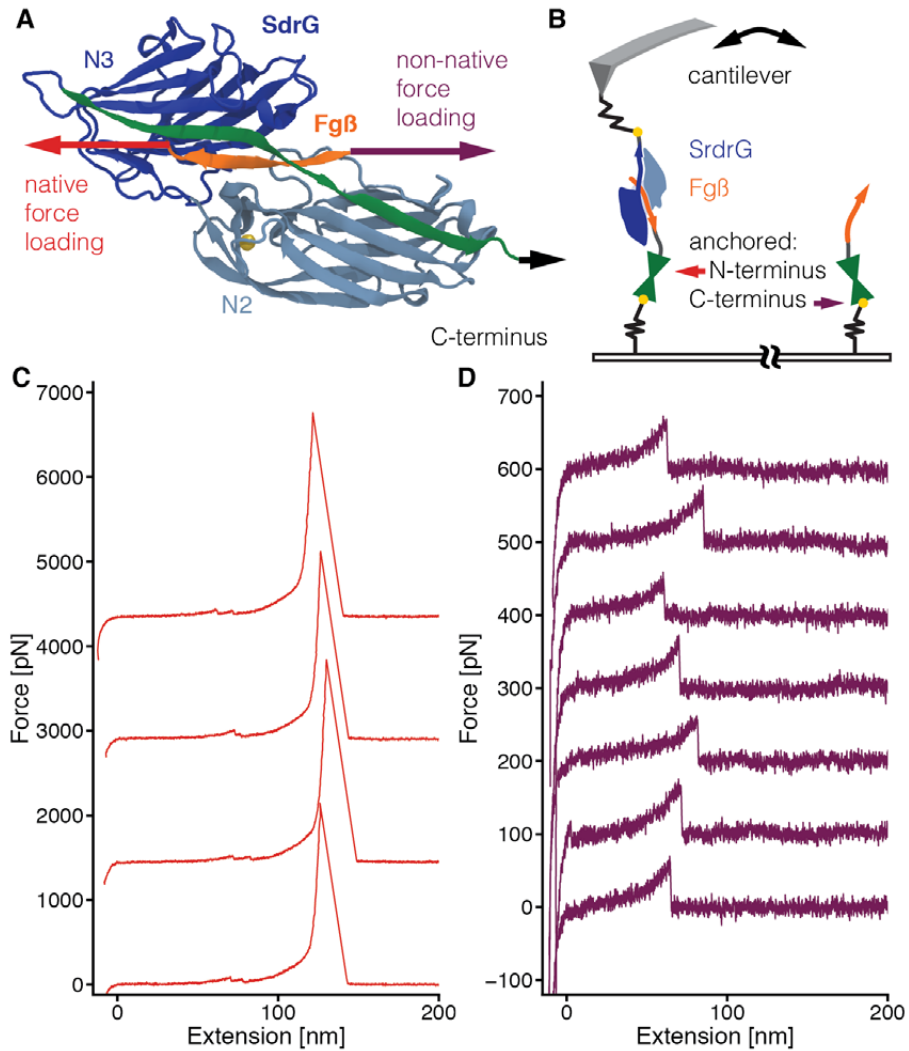
Fig. S15. Exemplary force traces in native and non-native configurations.
(A) Structure of the SdrG(blue):Fgß(orange) complex with the locking strand connecting the Ig-fold N2 and N3 domains (green). The SdrG C-terminus is natively tethered (black arrow) as it connects to the bacterium. In the native force loading configuration for Fgß, the peptide is tethered from its C-terminus (red arrow), where fibrinogen continues. The non-native tethering from the Fgß N-terminus is shown as purple arrow. (B) Experimental setup of a multispot measurement: the cantilever is alternated between spatially separated spots with the native (Fgß at C-terminus) and non-native (Fgß at N-terminus) configurations, allowing an absolute comparison of rupture forces, as a single force probe is used. (C) Exemplary resulting force extension traces at 1.6 µm s^{-1} retraction velocity for the native, high-force configuration, offset in force for readability. Notably, the ddFLN4 fingerprint unfolds at low forces and the complex breaks above 2 nN. (D) Exemplary force extension traces form the non-native configuration at 1.6 µm s^{-1} retraction velocity. The complex rupture occurs around 60 pN, significantly weaker compared to (C) and not sufficient to unfold the ddFLN4 fingerprint.
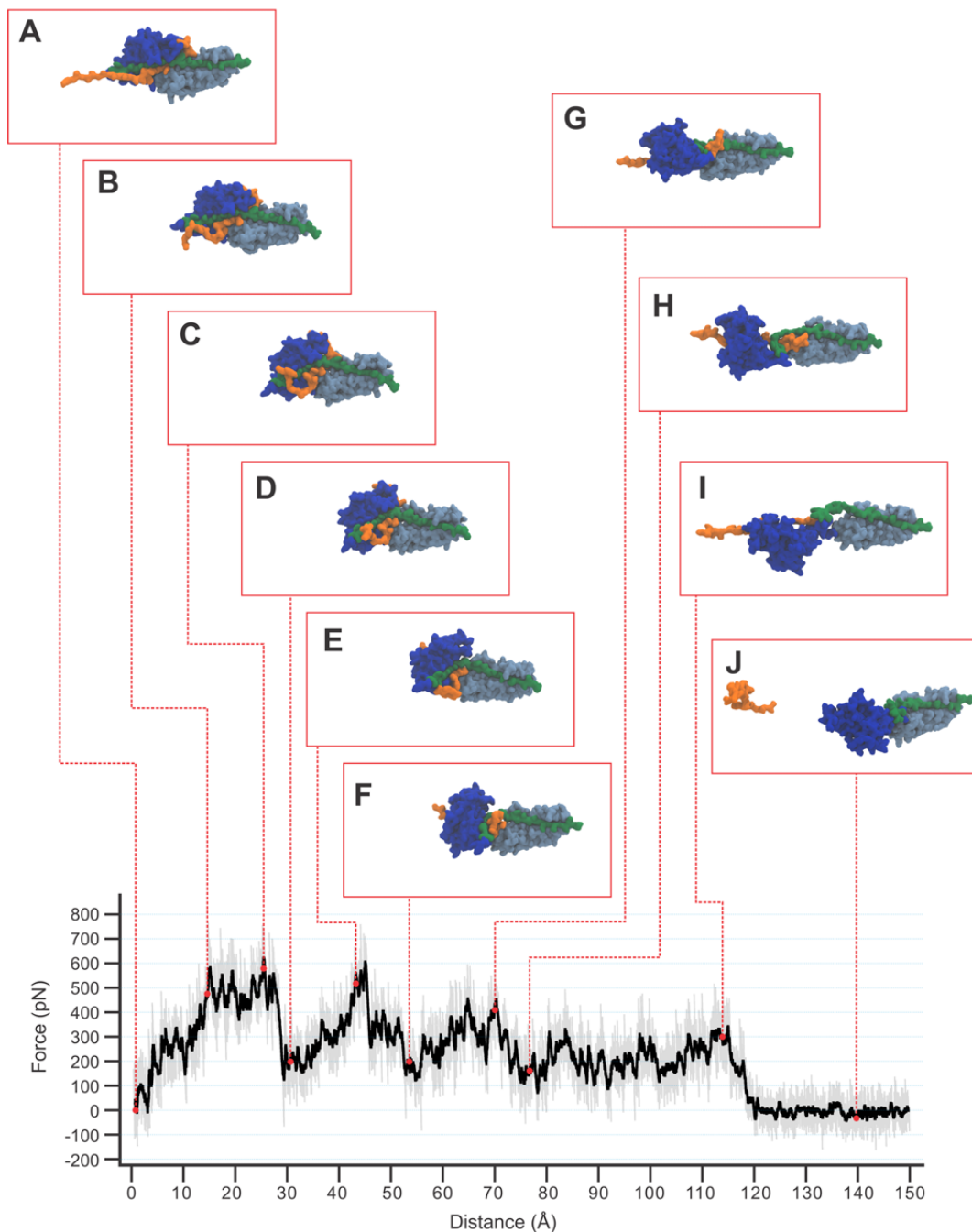
Fig. S16. SMD force-extension trace with equivalent structure snapshots for non-native pulling.

SMD force-extension trace in the non-native geometry of SdrG:Fgß (orange) including experimental peptide linkers including simulation snapshots (A-J). No clear force peak is discernible, as opposed to the native configuration (see Fig 1F). Notably, the contact between N2 (light blue) and N3 (dark blue) domain is "cracked" open, the H-bonds to the locking strand (green) are not set in a cooperative geometry, and so the peptide can be unzipped from the binding pocket as the H-bonds are now broken individually – resulting in the significantly weaker overall forces.
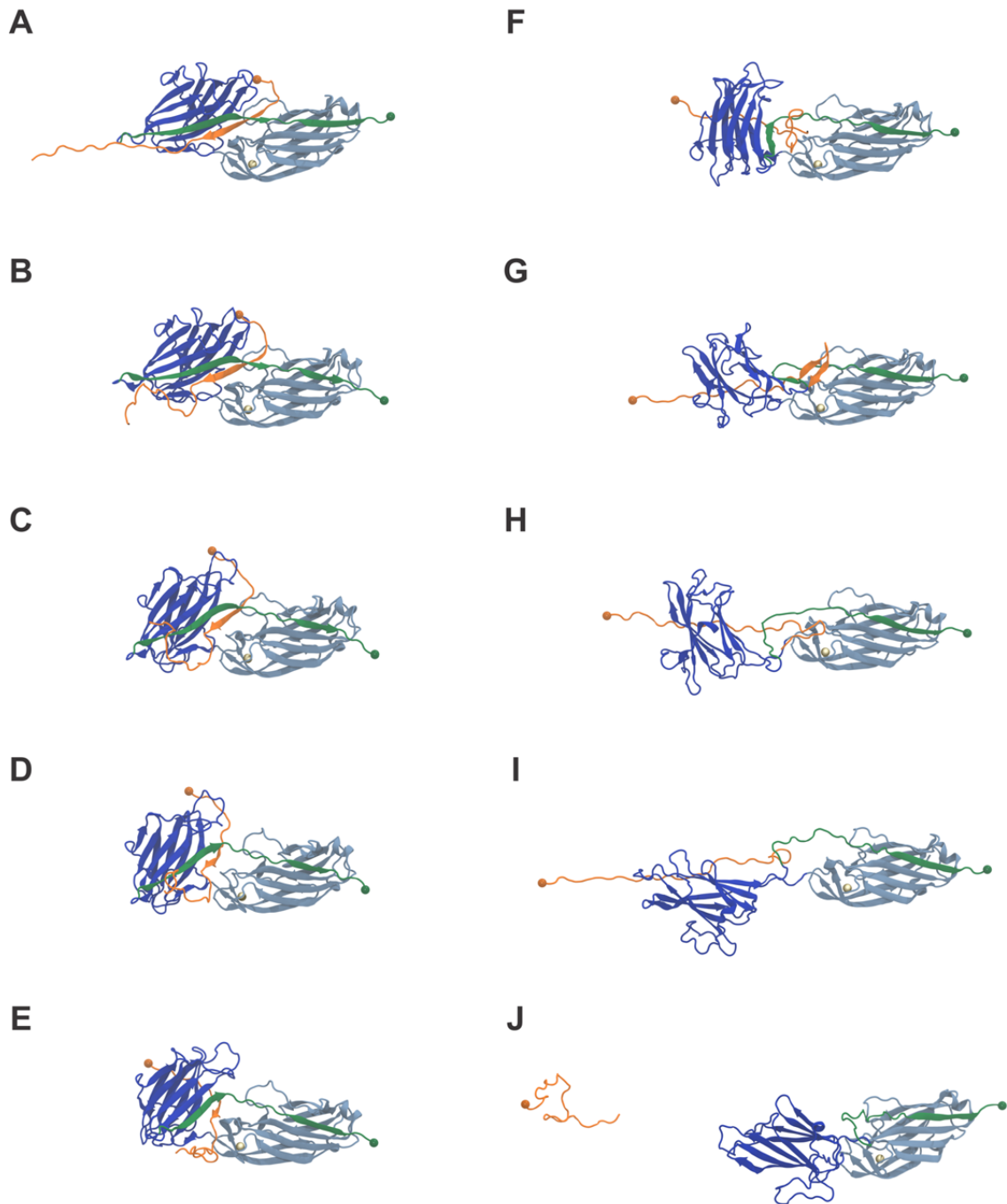
Fig. S17. Snapshots from non-native pulling SMD.
Representation of the evolution of SdrG (blues):Fgß (orange) structure during a non-native pulling steered molecular dynamics simulation. Snapshots (A-J) refer to steps from Fig. S16.
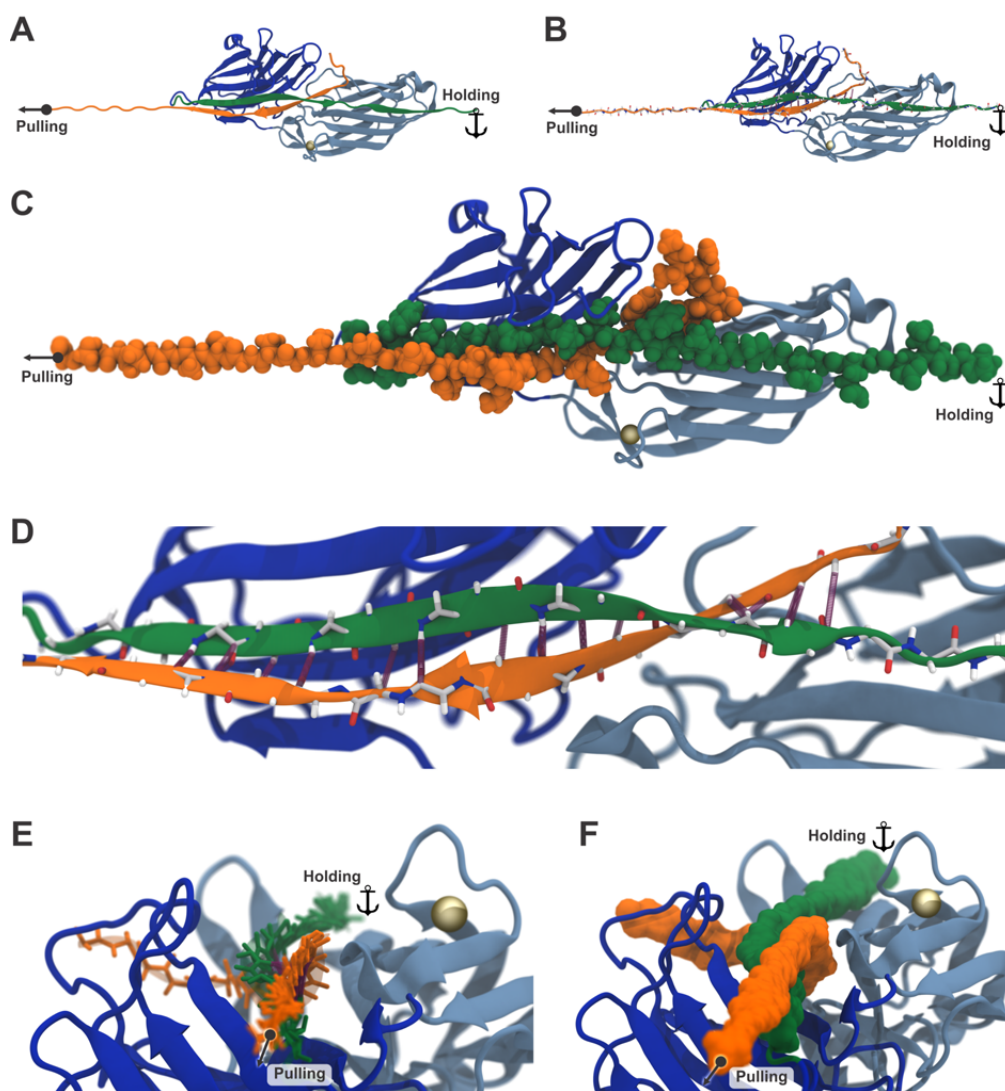
Fig. S18. Representation of the corkscrew arrangement of SdrG with full-length Fgß peptide under force load.

(A) Secondary structure of the SdrG(blue):Fgß(orange) complex with the locking strand (green) connecting the Ig-fold N2 (light blue) and N3 (dark blue) domains. Modeller and VMD/QwikMD were employed to model the complete Fgß peptide, including experimental peptide linkers (GTNEEGFFSARGHRPLDGSGSGSGSAGTGSG), in the SdrG pocket, using the crystal structure of the SdrG:Fgß complex as template. (B) Hydrogen bonds between SdrG and Fgß are represented in purple. Backbone atoms are represented by sticks colored by atom element. (C) Detailed view of the SdrG:Fgß interface. (D) Magnified view of the screw-like arrangement of all H-bonds formed by the complete peptide, also those with a stretch of the locking strand that is part of the N3 domain. (E-F) From the pulling axis perspective an arrangement reminiscent of a corkscrew in a cork reveals how the two beta strands lock each-other in a strong, cooperative shear geometry that is able to withstand the extreme forces measured.
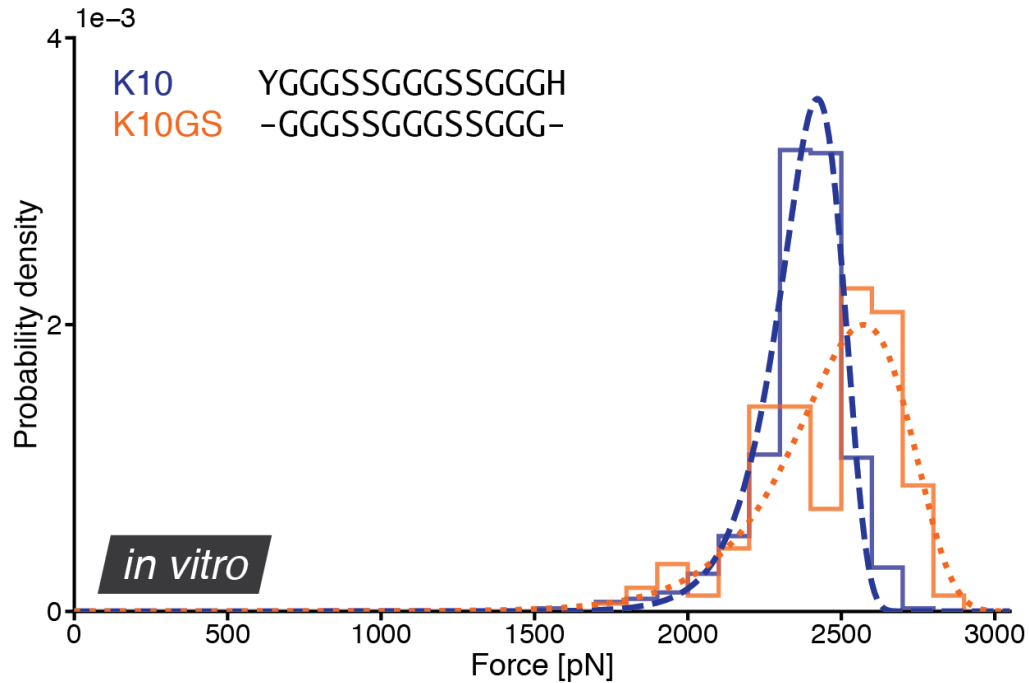
Fig. S19. ClfB binds a reduced, purely glycine-serine version of K10 with forces larger than 2 nN.

ClfB binds the K10 peptide with forces over 2 nN (blue, dahed line, N = 457). A truncated version of K10 consisting of only glycines and serines named K10GS, reaches similar, even slightly higher forces (orange, dotted line, N = 182) when both are compared with a single cantilever. These results support the largely side chain independent mechanics, as K10GS can be seen as a flexible linker region and likely has no special secondary structure nor any bulky, charged or especially hydrophobic side chains.

Table S1. Overview of all SMD simulations of SdrG and its homologs.

Summary of all steered molecular dynamics simulations performed with SdrG. A total of 2483 simulations were conducted, accounting for over 45 µs of all-atom molecular dynamics simulations. SMD simulations were performed using nearly 30 million processor-hours of GPU accelerated XK nodes of the NCSA/Blue Waters supercomputer.

ID	System Description	Holding	Pulling	\Number of Simulation Replicas per Pulling Speed (Å/ns)										High Force		Details
				250	125	50	25	12.5	2.5	1.25	0.5	0.25	0.05	in +Z	in -Z	
0	FgßF3 - SdrG bound to fibrinopeptide B: GFFFSARGHRP (PDB: 1R17)	PRO596	PRO18				2		102	1	1		2	YES	YES	
1	SdrG with longer peptide: GGFFGGGGGGGGGGGGGGGGGGGFFFSARGHRP	PRO596	PRO31				1		1		1			YES	YES	
2	FgßF2 - SdrG with mutated fibrinopeptide B (F9G): GGFFSARGHRP	PRO596	PRO18	101			101		101		1			YES	YES	
3	FgßF1 - SdrG with mutated fibrinopeptide B (F9G & F10G): GGGFSARGHRP	PRO596	PRO18				1		101		1			YES	YES	
4	FgßF0 - SdrG with mutated fibrinopeptide B (F9G & F10G & F11G): GGGGSARGHRP	PRO596	PRO18				1		101		1			YES	YES	
5	SdrG with very long peptide: MATFFSGTGTAGGTGSGSGTGSGGGSFFFGSGSAGGSGSGSSGGSSGASGTGTAGTAGGTGSGSGTGSSGGGSGGGSNEEGFFSARGHRP	PRO597	PRO90				2		1		1			YES	YES	
6	SdrG with truncated, short peptide: SARGHRP	PRO598	PRO18				1		1		1			YES	YES	
7	SdrG bound to fibrinopeptide B: GFFFSARGHRP (PDB: 1R17)	LYS379	PRO18				1		1		1			YES	YES	not clear peak
8	SdrG bound to fibrinopeptide B: GFFFSARGHRP (PDB: 1R17)	GLY276	PRO18				1		1		1			YES	YES	not clear peak
9	SdrG with mutated fibrinopeptide B: GFFFGGGGGGG	PRO596	GLY18				1		1					YES	YES	
10	SdrG with mutated fibrinopeptide B: GFFFSARGGGG	PRO596	GLY18				1		1					YES	YES	
11	SdrG with mutated fibrinopeptide B: GFFFGGGGHRP	PRO596	PRO18				1		1					YES	YES	
12	SdrG with truncated (thrombin cleaved) fibrinopeptide B: GHRP	PRO596	PRO18				1		1					NO	NO	
13	Truncated SdrG (N-terminal to GLN589 ...FSTSSGQ) with fibrinopeptide B	GLN589	PRO18				1		51					YES	YES	
14	Truncated SdrG (N-terminal to THR580 ...TASYDNT) with fibrinopeptide B	THR580	PRO18				1		51					NO	NO	
15	SdrG with "inverted sequence" fibrinopeptide B: PRHGRASFFFG: GLY8 becomes PRO8, PHE9 becomes ARG9, PHE10 becomes HIS10, ...	PRO596	PRO8				1		1					NO	NO	
16	SdrG with mutated (all-GLY) peptide: GGGGGGGGGG	PRO596	GLY18				1		101					YES	YES	not clear in -Z
17	SdrG with truncated fibrinopeptide B: FFFSARGHRP	PRO596	PRO18				1		51					YES	YES	
18	SdrG with truncated fibrinopeptide B: FFSARGHRP	PRO596	PRO18				1		51					YES	YES	
19	SdrG with truncated fibrinopeptide B: FSARGHRP	PRO596	PRO18				1		51					YES	YES	
20	SdrG with truncated fibrinopeptide B: SARGHRP	PRO596	PRO18				1		51					YES	YES	
21	SdrG with truncated fibrinopeptide B: ARGHRP	PRO596	PRO18				1		51					YES	YES	
22	SdrG with truncated fibrinopeptide B: RGHRP	PRO596	PRO18				1		51					NO	NO	
23	Truncated SdrG (N-terminal to THR580 ...TASYDNT) with fibrinopeptide B	LYS379	PRO18				1		1					NO	NO	
24	SdrG with "inverted sequence" fibrinopeptide B: PRHGRASFFFG: GLY8 becomes PRO8, PHE9 becomes ARG9, PHE10 becomes HIS10, ...	PRO596	GLY18				1		1					YES	YES	not clear in -Z
25	Truncated SdrG (N-terminal to GLN589 ...FSTSSGQ) with fibrinopeptide B	LYS379	PRO18				1		1					YES	YES	not clear in +Z
26	Mutated SdrG (PRO399 and ASP499 to GLY) with fibrinopeptide B	PRO596	PRO18				1		1					YES	YES	
27	Mutated SdrG (SER396 and TYR504 to GLY) with fibrinopeptide B	PRO596	PRO18				1		1					YES	YES	
28	Mutated SdrG (PRO399 and ASP499 to GLY) with fibrinopeptide B	PRO596	PRO18				1		1					YES	YES	
29	Mutated SdrG (PRO399 and SER500 to GLY) with fibrinopeptide B	PRO596	PRO18				1		1					YES	YES	
30	Mutated SdrG (LYS395, PRO399, ASN400, ASP499 and SER500 to GLY) with fibrinopeptide B	PRO596	PRO18				1		1					YES	YES	
31	SdrG with extra bond (PRO399 - ASP499) with fibrinopeptide B	PRO596	PRO18				9		1					YES	YES	not clear in -Z
32	SdrG with extra bond (SER396 - TYR504) with fibrinopeptide B	PRO596	PRO18				1		1					YES	YES	
33	SdrG with extra bonds [(PRO399 - ASP499) and (SER396 - TYR504)] with fibrinopeptide B	PRO596	PRO18				1		22					YES	YES	not clear in -Z
34	SdrG bound to fibrinopeptide B: GFFFSARGHRP (PDB: 1R17) - Holding everything but 5A always from peptide	SdrG	PRO18				1		1					YES	YES	not clear in -Z
35	SdrG bound to fibrinopeptide B: GFFFSARGHRP (PDB: 1R17) - changing the charges of part (residues 9 to 15: FFFSARG) of the peptide backbone to Zero	PRO596	PRO18				1		51					YES	YES	smaller in -Z
36	SdrG bound to fibrinopeptide B: GFFFSARGHRP (PDB: 1R17) - changing the charges of the peptide backbone to Zero	PRO596	PRO18				1		51					YES	NO	
37	SdrG bound to fibrinopeptide B: GFFFSARGHRP (PDB: 1R17) - changing the charges of the whole peptide to Zero	PRO596	PRO18				1		51					YES	NO	
38	SdrG with mutated (all-GLY) peptide: GGGGGGGGGG - changing the charges of the whole peptide to Zero	PRO596	PRO18				1		51					NO	NO	
39	SdrG bound to shortened fibrinopeptide B: FFSARGC (PDB: 1R17)	PRO596	CYS16						51					YES	YES	
40	SdrG with full peptide sequence, same as in the experiment: GTNEEGFFSARGHRPLDGSGSGSGSAGTGSG	PRO596	GLY34		200	200	200	100	101			100		YES	YES	
41	SdrG with full peptide sequence, same as in the experiment: GTNEEGFFSARGHRPLDGSGSGSGSAGTGSG	PRO596	GLY4						51					NO	NO	
42	FgßF2 - SdrG with mutated fibrinopeptide B (F9G): GGFFSARGHRP	PRO596	GLY8						51	5			1	NO	NO	

Movie S1.

A summary of the molecular mechanism responsible for WT SdrG:Fgß's extreme mechanostability from *in silico* steered molecular dynamics simulations.

Movie S2.

Representative steered molecular dynamics simulation of the SdrG:Fgß complex in the weaker non-native pulling configuration.

Supplementary References

1. D. G. Gibson *et al.*, Enzymatic assembly of DNA molecules up to several hundred kilobases. *Nat. Methods.* **6**, 343–345 (2009).
2. J. Yin *et al.*, Genetically encoded short peptide tag for versatile protein labeling by Sfp phosphopantetheinyl transferase. *Proc. Natl. Acad. Sci. U. S. A.* **102**, 15815–20 (2005).
3. F. W. Studier, Protein production by auto-induction in high-density shaking cultures. *Protein Expr. Purif.* **41**, 207–234 (2005).
4. M. A. Jobst, C. Schoeler, K. Malinowska, M. A. Nash, Investigating Receptor-ligand Systems of the Cellulosome with AFM-based Single-molecule Force Spectroscopy. *J. Vis. Exp.*, 1–10 (2013).
5. W. Ott, M. A. Jobst, C. Schoeler, H. E. Gaub, M. A. Nash, Single-molecule force spectroscopy on polyproteins and receptor–ligand complexes: The current toolbox. *J. Struct. Biol.* (2016), doi:10.1016/j.jsb.2016.02.011.
6. T. Verdorfer *et al.*, Combining in Vitro and in Silico Single-Molecule Force Spectroscopy to Characterize and Tune Cellulosomal Scaffoldin Mechanics. *J. Am. Chem. Soc.* **139**, 17841–17852 (2017).
7. J. L. Hutter, J. Bechhoefer, Calibration of Atomic-Force Microscope Tips. *Rev. Sci. Instrum.* **64**, 1868–1873 (1993).
8. H. Butt, M. Jaschke, Calculation of thermal noise in atomic force microscopy. *Nanotechnology.* **1** (1995).
9. J. D. Hunter, Matplotlib: A 2D Graphics Environment. *Comput. Sci. Eng.* **9**, 90–95 (2007).
10. F. Pedregosa *et al.*, Scikit-learn: Machine learning in Python. *J. Mach. Learn. Res.* **12**, 2825–2830 (2011).
11. S. van der Walt, S. C. Colbert, G. Varoquaux, The NumPy Array: A Structure for Efficient Numerical Computation. *Comput. Sci. Eng.* **13**, 22–30 (2011).
12. L. Condat, A Direct Algorithm for 1-D Total Variation Denoising. *IEEE Signal Process. Lett.* **20**, 1054–1057 (2013).
13. L. Rudin, S. Osher, E. Fatemi, Nonlinear total variation based noise removal algorithms. *Phys. D Nonlinear Phenom.* **60**, 259–268 (1992).
14. L. Livadaru, R. R. Netz, H. J. Kreuzer, Stretching Response of Discrete Semiflexible Polymers. *Macromolecules.* **36**, 3732–3744 (2003).
15. E. M. Puchner, G. Franzen, M. Gautel, H. E. Gaub, Comparing proteins by their unfolding pattern. *Biophys. J.* **95**, 426–34 (2008).
16. T. Hugel, M. Rief, M. Seitz, H. Gaub, R. Netz, Highly Stretched Single Polymers: Atomic-Force-Microscope Experiments Versus Ab-Initio Theory. *Phys. Rev. Lett.* **94**, 48301 (2005).
17. B. Silverman, Density Estimation for Statistics and Data Analysis. *Monogr. Stat. Appl. Probab.* **37**, 1–22 (1986).
18. S. Izrailev, S. Stepaniants, M. Balsera, Y. Oono, K. Schulten, Molecular dynamics study of unbinding of the avidin-biotin complex. *Biophys. J.* **72**, 1568–1581 (1997).
19. E. Evans, K. Ritchie, Dynamic strength of molecular adhesion bonds. *Biophys. J.* **72**, 1541–55 (1997).

20. O. Dudko, G. Hummer, A. Szabo, Intrinsic Rates and Activation Free Energies from Single-Molecule Pulling Experiments. *Phys. Rev. Lett.* **96**, 108101 (2006).

21. K. Ponnuraj *et al.*, A "dock, lock, and latch" Structural Model for a Staphylococcal Adhesin Binding to Fibrinogen. *Cell.* **115**, 217–228 (2003).

22. V. K. Ganesh *et al.*, Structural and Biochemical Characterization of Staphylococcus aureus Clumping Factor B/Ligand Interactions. *J. Biol. Chem.* **286**, 25963–25972 (2011).

23. J. V Ribeiro *et al.*, QwikMD — Integrative Molecular Dynamics Toolkit for Novices and Experts. *Nat. Publ. Gr.* **6**, 1–14 (2016).

24. J. C. Phillips *et al.*, Scalable molecular dynamics with NAMD. *J. Comput. Chem.* **26**, 1781–1802 (2005).

25. R. B. Best *et al.*, Optimization of the Additive CHARMM All-Atom Protein Force Field Targeting Improved Sampling of the Backbone phi, psi and Side-Chain chi(1) and chi(2) Dihedral Angles. *J. Chem. Theory Comput.* **8**, 3257–3273 (2012).

26. W. L. Jorgensen, J. Chandrasekhar, J. D. Madura, R. W. Impey, M. L. Klein, Comparison of simple potential functions for simulating liquid water. *J. Chem. Phys.* **79**, 926 (1983).

27. T. Darden, D. York, L. Pedersen, Particle mesh Ewald: An $N \cdot \log(N)$ method for Ewald sums in large systems. *J. Chem. Phys.* **98**, 10089 (1993).

28. R. C. Bernardi, M. C. R. Melo, K. Schulten, Enhanced sampling techniques in molecular dynamics simulations of biological systems. *Biochim. Biophys. Acta - Gen. Subj.* (2014), doi:10.1016/j.bbagen.2014.10.019.

29. B. C. Goh *et al.*, Computational Methodologies for Real-Space Structural Refinement of Large Macromolecular Complexes. *Annu. Rev. Biophys.* **45** (2016).

30. A. Šali, T. L. Blundell, Comparative Protein Modelling by Satisfaction of Spatial Restraints. *J. Mol. Biol.* **234**, 779–815 (1993).

31. B. Webb, A. Sali, in *Methods in Molecular Biology Protein Structure Prediction*, D. Kihara, Ed. (Humana Press, New York, NY, ed. 3rd, 2014), vol. 1137, pp. 1–15.

32. F. Rico, L. Gonzalez, I. Casuso, M. Puig-Vidal, S. Scheuring, High-Speed Force Spectroscopy Unfolds Titin at the Velocity of Molecular Dynamics Simulations. *Science (80-.).* **342**, 741–743 (2013).

33. W. Humphrey, A. Dalke, K. Schulten, VMD: Visual molecular dynamics. *J. Mol. Graph.* **14**, 33–38 (1996).

34. M. Scheurer *et al.*, PyContact: Rapid, Customizable and Visual Analysis of Non-Covalent Interactions in MD Simulations. *Biophys. J.* (2018), doi:10.1016/j.bpj.2017.12.003.

35. A. Sethi, J. Eargle, A. A. Black, Z. Luthey-Schulten, Dynamical networks in tRNA:protein complexes. *Proc. Natl. Acad. Sci. U.S.A.* **106**, 6620–6625 (2009).

36. C. Schoeler *et al.*, Mapping Mechanical Force Propagation through Biomolecular Complexes. *Nano Lett.* **15**, 7370–7376 (2015).

37. U. Sridharan, K. Ponnuraj, Isopeptide bond in collagen- and fibrinogen-binding MSCRAMMs. *Biophys. Rev.* **8**, 75–83 (2016).